Faculdade de Engenharia da Universidade do Porto
Mestrado Integrado em Engenharia Mecânica

Parametric Study for the Optimal Pressure Tap Design in Microchannels

by

Tomás Rodrigues Pinto

Supervisor:
Laura Campo-Deaño
Assistant Professor, Faculty of Engineering, University of Porto

Co-Supervisor:
Francisco José Galindo-Rosales
Assistant Researcher, Faculty of Engineering, University of Porto

A THESIS
Submitted in partial fulfillment of the requirements
for the degree of
Master in Mechanical Engineering

July 2018

Â minha mãe e avó

'Whether you think you can, or think you can't, you're right'

Henry Ford

Abstract

The recent advances in microfabrication techniques allowed the use of microfluidics for characterising the complex flow dynamics around different microbot prototypes to be used in biomedicine. However, the complete fluid flow characterisation must include the determination of the pressure drop induced by the presence of these prototypes in order to assess the dynamic efficiency of these microdevices. Pressure measuring within microchannels poses serious challenges for the average experimentalist. Air bubbles and surface tension phenomena are quite frequent at this scale, and are known to seriously impact the quality of pressure measurements. Driven by this, the specific objective of this thesis is to study the influence of different shape parameters on the design of pressure taps in microchannels. Polydimethylsiloxane (PDMS) microchannels were fabricated, with different 2D microbot models inside. A wide range of pressure tap configurations was defined by varying three key shape parameters: sub-channel width, w; tap cross-section transition radius of curvature, R; tap cross-section transition angle of inclination, α. Pressure drop measurements were carried out with de-ionised (DI) water and compared to theory in order to determine the optimal tap design. Configurations with smooth contours, R, and sub-channel width, w, of 108 μm performed the best. Results from that of radius $R = 50$ μm only failed theory by ~5 %, making this the optimal shape within the conditions of the study.

Keywords: Microchannels. Pressure drop. Pressure taps. Microbots.

Resumo

Os recentes avanços no desenvolvimento de técnicas de microfabricação permitiram usar a microfluídica como plataforma para o estudo da dinâmica do escoamento em torno de protótipos de microrobôs para aplicações biomédicas. Uma análise detalhada da dinâmica do escoamento implica necessariamente a determinação da queda de pressão provocada por estes microrobôs. Tal informação, é pois crucial para a avaliação da eficiência dinâmica destes dispositivos. À determinação experimental de quedas de pressão em microcanais estão associados inúmeros problemas que adulteram os valores das medições, desde bolhas de ar a fenómenos de tensão superficial. Posto isto, surge a necessidade de encontrar uma solução viável para a medição de pressão em microcanais, capaz de conduzir a resultados com qualidade e de fácil implementação. O objetivo da presente tese é então, analisar a influência de vários parâmetros geométricos na forma de tomadas de pressão em microcanais e a repercussão destes na qualidade das medições. Para isso, foram fabricados microcanais de dimetil polissiloxano (PDMS) com diferentes protótipos de microrobôs no seu interior. A forma das tomadas de pressão foi variada de acordo com os seguintes parâmetros geométricos: largura do sub-canal, w; raio de curvatura, R; ângulo de inclinação, α. Foram efetuadas medições de quedas de pressão com água destilada e os resultados obtidos foram comparados com a teoria. As configurações de contornos suaves (transições de secção suaves), R, e largura de sub-canal, w, igual a 108 µm apresentaram os melhores resultados. Destas, aquela com raio de curvatura $R = 50$ µm mostrou ser a configuração ótima, ao registar resultados experimentais com um erro médio face ao perfil teórico inferior a 5 %.

Palavras-chave: Microcanais. Queda de pressão. Tomadas de pressão. Microrobôs.

Agradecimentos

Ao concluir este trabalho gostaria de manifestar os meus profundos agradecimentos a todos aqueles que de alguma forma contribuíram para a sua realização.

O meu sincero muito obrigado, à minha orientadora, a Professora Laura Campo-Deaño, não só pela oportunidade de desenvolver este projeto, mas também pelo empenho e acompanhamento constante e incondicional proporcionado durante todas as fases do trabalho. Agradeço sobretudo, toda a motivação e pronta disponibilidade com que sempre me recebeu. Obrigado por me ter guiado ao longo de todas as etapas, por ter acreditado em mim e pela sua amizade.

Quero também expressar os meus agradecimentos ao meu co-orientador, o Doutor Francisco Galindo-Rosales, pelo apoio incondicional dado durante os trabalhos experimentais e não só. Obrigado pela dedicação, motivação nos momentos mais difíceis e pelos conselhos amigos, os quais guardo comigo para a vida.

Agradeço a ambos, as oportunidades e experiências únicas que me proporcionaram ao longo deste período. Sem o apoio, os ensinamentos e a amizade dos dois, este trabalho não teria sido possível.

Uma palavra de especial reconhecimento à minha mãe e à minha avó, pela forma incondicional e constante com que sempre acreditaram e me apoiaram nesta caminhada e a quem exprimo profunda gratidão pela educação e instrução que me proporcionaram. Obrigado pelo estímulo e encorajamento, tão importantes nos momentos mais difíceis, e que ajudaram a ultrapassar as dificuldades do dia a dia. Se até aqui cheguei, devo-o a vocês. Estendo ainda estes agradecimentos aos restantes membros da minha família.

Agradeço também o bom acolhimento proporcionado pelos membros da sala L401, onde desenvolvi grande parte da escrita da tese. Em particular, aos Professores Carlos Rodrigues e Alexandre Afonso, ao Investigador Saeed Parvar e ao Doutor Ahmad Fakhari pelo apoio, amizade e boa disposição. Deixo ainda uma nota de agradecimento ao Professor Fernando Pinho, que de certa forma motivou o meu envolvimento neste projeto.

Um grande abraço e um obrigado a todos os meus amigos que me acompanharam ao longo deste percurso, por estarem sempre por perto e por percorrerem este caminho comigo, ajudando a que não me desviasse dele.

Por fim, agradeço ao Centro de Estudos de Fenómenos de Transporte (CEFT) a disponibilidade para a construção da instalação experimental e as condições e meios dispensados para a realização do trabalho.

Queria também agradecer a todas as pessoas que de uma forma inconsciente me esqueci de mencionar neste texto.

Tomás Rodrigues Pinto

Contents

List of Figures

List of Tables

Introduction

Microbots have come to be developed for, among other purposes, industrial applications and biomedicine (Martínez-Aranda *et al.*, 2016). In the biomedicine field, once the technology matures, microbots will allow for precise and delicate, minimally invasive procedures throughout the human body. As a matter of fact, the use of these microdevices as surgical tools will most certainly revolutionise areas such as cancer-fighting (Martel, 2012), drug delivery (Zhu *et al.*, 2015) and intraocular oxygen-sensing (Ergeneman *et al.*, 2012). Moreover, several patient-oriented benefits are to be expected given the minimally invasive nature of this surgical solution. Some of the expected benefits are related to the reduction of recovery time, risk of infection and medical complications (Mack, 2001, Carrozza *et al.*, 2003).

In order to further develop this technology, the dynamic efficiency and flow performance of microbots inside the human body are key topics that need to be fully grasped. A pioneering study (Martínez-Aranda *et al.*, 2016) developed a micro-hydrodynamic tunnel for the fluid flow characterisation of different microbot prototypes. The authors fully characterised the kinematics of the flow around the microbots with μPIV technology. However, the dynamics of the flow were not entirely characterised due to the intrinsic difficulties associated with measuring the pressure drop originated by the presence of the prototypes.

Despite the need for precise pressure measurements in microfluidics, the number of studies in this field is limited (Grundmann *et al.*, 2015). Mostly because pressure measuring at the micro scale is not particularly easy. Several problems have been reported, a great number of these associated with pressure tap design issues. For instance, one of the most frequent is the housing of air bubbles inside the taps or within the sub-channels that lead to them. These affect the accuracy of the readings tremendously, significantly distorting the final pressure results. Surface tension issues are also quite common, caused by the high surface area–volume ratios characteristic of microfluidic devices. Problems like these are frequently related to poorly designed pressure sensing structures with long and narrow sub-channels, which promote such undesired effects.

This study aims to minimise such difficulties when measuring pressure drops in microchannels,

by developing guidelines for the design of well functioning pressure taps and ultimately proposing an optimal tap configuration. For that reason, this thesis will consist on a preliminary simplified study, in which only distilled water (a Newtonian fluid) as the working fluid and microchannels without microbot prototype inside, will be tested.

This thesis is divided into four chapters:

Chapter 1 begins with a brief description of the motivation for the thesis and main objectives. Then, a general introduction to the field of microfluidics and some particularities of fluid flow at the micro scale are presented. Also, some considerations are made on the present and future of microbot technology as a tool for minimally invasive medicine. To conclude, several works in which pressure measurements were carried out within microfluidic devices are presented, and briefly described.

Chapter 2 gathers all the information about design, fabrication and experimentation. Hence, from design choices to flow regimes, all the details regarding the 'how' and the 'with what' any part of the experimental work played out can be found there.

Chapter 3 is where all the experimental results obtained are presented and discussed. A thorough discussion on the errors that might have affected the measurements unfolds in parallel.

Chapter 4 summarises the conclusions drawn in the previous Chapter. Prospects for further work are also presented here.

1.1 Microfluidics

> **mi·cro·flu·id·ics** (*mī′krō flōo id′iks*) n. The science and engineering of systems in which fluid behaviour differs from conventional flow theory primarily due to the small length of the system (Bruus, 2008).

Microfluidics is the science and technology which deals with systems that process small amounts of fluid, using geometries with dimensions of tens to hundreds of microns (Campo-Deaño *et al.*, 2011). However, the important length-scale for microfluidics is not the overall device size but rather the length-scale that determines flow behaviour. In fact, the main advantage of microfluidics is using scaling laws and continuum breakdown for investigating new effects (Nguyen and Wereley, 2006), since certain fundamental differences can be observed between the behaviour of fluids moving in large channels and those flowing through micro scale channels (Whitesides, 2006). Therefore, the microscopic quantity of fluid in play is the key issue in microfluidics, not the size of the surrounding instrumentation. That said, the term 'microfluidics' is used throughout the text not only to link the fluid mechanics to the micro scale, but also to refer, in general, to situations in which small-size scale causes changes in fluid behaviour. For instance, with microfluidics, strong viscoelastic effects can be achieved in fluids that would otherwise behave essentially as Newtonian fluids in equivalent macro

scale flows (Rodd *et al.*, 2007, McKinley *et al.*, 2007). This is the case of low viscosity elastic fluids, whose subtle elastic character only displays at high deformation rates and low Reynolds numbers (*Re*), a condition practically impossible to reproduce at macro scale due to the dominant inertial effects. At micro scale though, the role of inertia is significantly diminished thanks to the small length-scales, and therefore experiments at high deformation rates whilst maintaining small *Re* flows can be carried out (Rodd *et al.*, 2007).

Back in the late 1970's, following up on the device miniaturisation trend set by Richard Feynman upon his 1959 speech 'There's Plenty of Room at the Bottom' (Feynman, 1992), silicon technology was extended to machining microelectromechanical systems, or MEMS, smaller than a millimetre mechanical devices (Kestenbaum *et al.*, 2002, Tabeling, 2005). With it, the first microfluidic devices appeared: micromechanical valves, micropumps, microflow sensors, etc. (Gravesen *et al.*, 1993, Shoji and Esashi, 1994). The success of silicon-based microelectronics lead to believe that microfluidics could also benefit from silicon technology, which it did but only at an early stage, since elastomers (such as polydimethylsiloxane, or PDMS) proved to be much more advantageous for microfluidic fabrication than rigid materials (e.g., silicon and glass) (Whitesides, 2006). In that sense, the development of microfluidics owes a lot to its predecessor technology, MEMS, that along with the introduction of rapid prototyping (Effenhauser *et al.*, 1997, Duffy *et al.*, 1998) and the following advances in microfabrication techniques, allowing the cheap, fast and reliable manufacture of micro scale geometries (Quake and Scherer, 2000, Ng *et al.*, 2002, Marrian and Tennant, 2003), have lead it to the state where is at today.

The microfluidics field is mainly driven by technological applications, such as molecular analysis (e.g., analysis of DNA molecules), biodefense (e.g., systems for dispensing therapeutic agents), molecular biology, microelectronics (e.g. inkjet printing heads), clinical diagnostics, and drug development (Whitesides, 2006), the vision being to develop entire bio/chemical laboratories on the surface of polymer chips, that operate as analytical devices able to perform all the required processes of a sample analysis: manipulation, transport, and control of small-sized fluid samples (e.g., biological samples), as well as detection and readout electronics (Gupta *et al.*, 2010, Tng *et al.*, 2015, Ahn *et al.*, 2004). When dealing with biological fluids these miniaturised laboratories are called *Lab-on-a-Chip* (LOC) systems, whereas for chemical fluids the correct designation is micro-total analysis systems, μTAS (Luttge, 2011). LOC systems can be thought of as the natural generalisation of MEMS (Bruus, 2008), however method development for these is still slow, being particularly hampered by the high investment costs for customised chip technologies compared to the well-established batch-based array-type assays in biology (Luttge, 2011). Other than that, several challenges still remain regarding the miniaturisation of these systems, such as the integration of actuation and sensing technologies (optical, electrochemical and acoustic) on a single chip, and the mixture, pumping,

transport, separation, and control of fluids at the micro scale level (Catarino *et al.*, 2017). Although, once fully developed *Lab-on-a-Chip* systems are expected to have a revolutionary impact in several scientific disciplines, such as biotechnology, pharmacology, medical diagnostics, forensics, environmental monitoring and basic research (Bruus, 2008, Whitesides, 2006, Scott, 2004).

Besides the more practical applications, microfluidics has renewed the interest in many of the fundamental problems of fluid mechanics which had already been long solved (Scott, 2004). The small characteristic length-scales give rise to surface tension phenomena, ultimately asking for a different approach towards the study of flow dynamics inside microchannels, since 'now' a pressure is required to drive liquid through these. For instance, the understanding of how different forces interact inside small microfluidic capillaries such that they can be used effectively for transportation is an important area of research (e.g., medical microbots for human body procedures, such as drug delivery and biological material removal (Nelson *et al.*, 2010)) (Luttge, 2011). Furthermore, microfluidics has opened a door in the study of complex fluids (e.g., blood), since these too behave differently at the micro scale, where viscous stresses dominate over inertia, as explained above. Not only that, but microfluidic techniques also present new opportunities for material property measurements, allowing to investigate the rheological responses of non-Newtonian fluids at smaller length-scales. Probing high deformation rates in the absence of inertia, measuring flow phenomena when device length-scales approach those of the underlying material's microstructure and the possibility of studying sample volumes on the order of nanolitres are just a few of the many advantages that hype the rheological potential in microfluidics (Pipe and McKinley, 2009). The numerical community has also taken up microfluidics, merging the small length-scales that characterise it with the research areas of complex and turbulent flows. And with increasing amounts of research focused on microfluidics, whether envisioning a practical application or strictly fundamental in nature, the potential reach of this technology becomes virtually unbounded.

1.1.1 Fluid flow in microchannels

Flows at the micro scale differ significantly from their macroscopic counterparts. The small characteristic length-scales generally result in fluid flows where viscous forces dominate over inertial effects, thus making interfacial phenomena and molecular effects much more important than gravity (Kirby, 2010). The theoretical assumption that fluids behave as continuous media, adopted in classical fluid mechanics, holds true for micro scale flows (Nguyen and Wereley, 2006). However, the continuum hypothesis breaks down when the system under consideration approaches the molecular scale (e.g., nanofluidics) (Bruus, 2008). Moreover, micro scale flows are typically laminar, even though turbulent regimes can still be achieved at larger Reynolds numbers - previous data on critical Reynolds numbers in rectangular cross-section microchannels set a laminar–turbulent transition

interval of $200 \leq Re \leq 2100$ (Hetsroni *et al.*, 2005).

The ratio of surface area (S) to volume (V) for a fluid element is proportional to $S/V \sim d^{-1}$, with d being its characteristic length-scale. Therefore, heading towards smaller length-scales increases the relative importance of surface interactions, compared to the fluid's behaviour as a bulk (Pipe and McKinley, 2009). Indeed, surface effects dominate the flow at micro scale, with surface tension exceeding body forces, such as gravity. Surface tension relates to surface contact angle through Young-Laplace's equation, which dictates that there must be balance between all surface tension forces acting at a given interface - i.e., at equilibrium these forces sum to zero. The contact angle for water drops in air on the surface of polydimethylsiloxane (PDMS) was measured to be anywhere in between 50–105°, at 20°C (Kirby, 2010). The classical 'no-slip' condition has been proved to hold true at small length-scales, both experimentally and numerically. Despite this, some interfacial effects triggered by surface interactions have been reported, mostly in the flow of polymer solutions. Surface irregularities (e.g., roughness) are possible causes for such phenomena (Lauga *et al.*, 2007, Voronov *et al.*, 2008).

Besides the ones here briefly introduced, more effects that are normally neglected when considering macro scale flow have been reported (see Figure 1.1). For further information on all, please refer to the authors cited throughout this subsection.

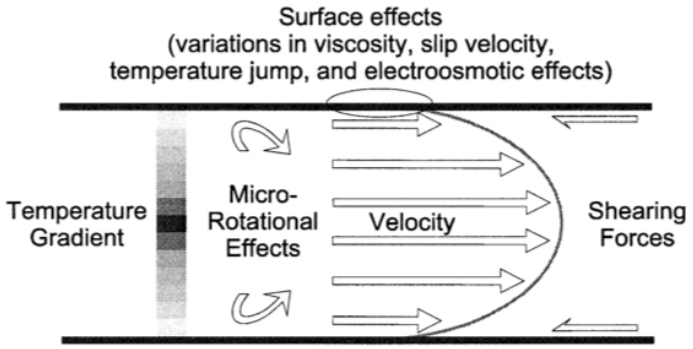

Figure 1.1: Schematic representation of various effects in micro scale flow (reprinted from Papautsky *et al.* (1999), with permission from Elsevier).

1.2 Medical microbots

The characterisation of the flow dynamics of microbots inside the human body, naturally includes the determination of the pressure drop caused by their sole presence inside the blood vessels. Driven by this need, in this work pressure drop measurements are carried out across vessel-like microchannels with no obstacles, the aim being to primarily develop a good strategy for getting these mea-

surements. For that reason, no complex fluids are considered. In order to explain the concept behind microbot technology, a brief description follows.

The notion that a surgeon's most important skill is cognitive ability has increasingly come to grow in the medical community. The technical skills required for precision and dexterity procedures can now often be delegated to appropriate technology (Nelson *et al.*, 2010).

That is where medical microbots come in. These micron-size robots can travel throughout the endless conduits of the human body performing delicate operations that would otherwise be necessarily more invasive. Thanks to their reduced dimensions, these microbots allow for interventions with minimal trauma and present several patient-oriented benefits, such as reduced recovery time, infection risk and postoperative pain (Mack, 2001). Once fully developed, these untethered, wirelessly controlled and powered devices will certainly make existing therapeutics and diagnostic procedures far less invasive and enable new procedures never before though possible (Nelson *et al.*, 2010).

Microbots are being design so that they are able to wirelessly navigate through the human circulatory system, urinary system and central nervous system. Once inside the human body, microbots will encounter a range of different environments through which to navigate along, all the way from fluid filled lumens and cavities to soft tissues (Nelson *et al.*, 2010). In that sense, designing a single microbot that is capable of negotiating such frequently changing environments is not an easy task. Furthermore, as one scales down to the microscale, although the fundamental physics governing the devices remains the same, the relative importance of physical effects changes, as already explained. In addition to that, the generation and storage of power, inherent problematics to the propulsion, movement, communication and data transmission of microbots, becomes increasingly difficult (Nelson *et al.*, 2010). These are the most challenging aspects about the development of this technology that need to be dealt with in the near future.

Microbots are believed to have the potential to revolutionise several aspects of modern medicine, not far from now. Despite having still a lot of ground ahead to cover and specific applications being only at an early concept stage, considering the rate at which the state of the art has been progressing one can safely assume that in the near future microbots will likely be carrying out relatively simple functions, while supervised or directly controlled by a clinician (Nelson *et al.*, 2010).

1.3 Pressure measurements within microfluidic devices

The most common pressure sensors used in microfluidics are capacitive (Lei *et al.*, 2012) and piezoresistive (Li *et al.*, 2010, Lee and Choi, 2008, Park *et al.*, 2007). Besides these, other variations, such as optical (Kohl *et al.*, 2005a,b) and resonant sensors, do exist. A general review of several pressure

sensing technologies for microdevices can be found in Eaton and Smith (1997). These days, piezoresistive pressure sensors with high preciseness and sensitivity are the ones that are most used. These are highly accurate when it comes to pressure sensing, can read both absolute and relative pressure in a wide measurement field and their handling is straightforward.

Besides the commercially available external pressure sensors, which are the most straightforward means for obtaining pressure data with little to none device design requirements, several other methods for determining pressure drops in microchannels have been reported. The base material from which the microchannels are made, for instance, thanks to its intrinsic properties, might allow for specific pressure measuring methods. That is the case of silicon-based microchannels, a rather decaying solution for microdevice fabrication thanks to the much practical and cheaper polydimethylsiloxane (PDMS) alternative. Several research groups (Kohl *et al.*, 2005b, Ateya *et al.*, 2005, Kuoni *et al.*, 2003) have used silicon-based microchannels, mainly because silicon can be routinely etched and therefore several sensing elements can be incorporated. The process of pressure drop measuring within silicon-based microdevices follows a different principle as that of PDMS-based ones. It involves reflecting an imposed laser beam upon a deflecting silicon channel wall and relating the reflection angle to the channel's pressure (Kohl *et al.*, 2005b). When it comes to pressure sensing with PDMS, several research groups (Chung *et al.*, 2009, Wu *et al.*, 2011, Hosokawa *et al.*, 2002, Kartalov *et al.*, 2007, Chang *et al.*, 2008, Hardy *et al.*, 2009) have used its elastic nature to their advantage, relating the deflection of the inner walls to the channel's pressure by means of imaging tools. However, this method and others alike often require additional fabrication steps (Hosokawa *et al.*, 2002) in order to incorporate extra channel layers into the main PDMS flow channels (Chung *et al.*, 2009, Wu *et al.*, 2011, Kartalov *et al.*, 2007, Chang *et al.*, 2008), fluorescent particles (Chung *et al.*, 2009, Hardy *et al.*, 2009), or even to introduce separate probing fluids (Wu *et al.*, 2011, Kartalov *et al.*, 2007).

Based on the principle of measuring pressure drop over an hydraulic resistor, Oosterbroek *et al.* (1999) developed a device that combines both a pressure and a flow rate sensors. Two prototypes were made, an hybrid piezoresistive and a capacitive. The authors claim it is a microfluidic device-friendly sensor, robust and simple in electronics. However, energy loss caused by friction effects and lack of compensation for viscosity induced temperature changes make it inadequate for high precision measurements.

Banerjee *et al.* (2014) set out to develop a pressure sensing system for microfluidic environments based on low-leakage microballoons. These compressible microballoons change their size in response to pressure changes. The applicability of this method and wether it is suitable or not for a particular situation, is determined by the diameter of the channel in which its implementation is desired. This is fundamentally due to the diameter of the microballoons (~17 μm). Thus, in chan-

nels with 10 μm diameter and less, for instance, using this technology would not be advisable, given the large amount of fluid that would need to go in the balloons, when compared to the amount in circulation.

Park *et al.* (2007) developed a carbon fibre-based piezoresistive pressure sensor. While conventional piezoresistive pressure sensors have four diffused silicon wire sensing piezoresistors in a closed Wheatstone bridge configuration, in the one here conceived these piezoresistors are replaced with carbon fibres. Compared to silicon wire, carbon fibres are easier to fabricate and have higher gauge factor, thus proving to be an interesting solution for pressure measuring systems.

Another carbon fibre-based piezoresistive pressure sensor was developed by Lee and Choi (2008), this time with a PDMS diaphragm instead of the conventional silicon one. Here, not only do the piezoresistors get replaced by carbon fibres (the new sensing elements of the sensor), but also the diaphragm is different. With a PDMS diaphragm, larger deformations under low pressure are possible, since its Young's modulus is greater than that of silicon. The PDMS diaphragm was 50 μm-thick and the carbon fibres were manufactured from polyactylonitrile (PAN).

Kohl *et al.* (2005b) carried out pressure measurements by an optical membrane-based method, in order to determine friction factors. The experimental friction factors obtained were compared to those predicted by laminar conventional theory.

Following up on their previous work, a microfluidic platform with internal pressure measurements was described by Kohl *et al.* (2005a). In this platform, the deformation of silicon membranes (placed inside small sub-channels that lead from a main flow channel) with pressure is read through an optical laser-based process. These deformations are then converted to pressure. The silicon membranes developed are electronics-free, so no piezoresistors or capacitors are required. As explained at the beginning, internal measuring systems often require extra fabrication steps in order to be incorporated into microdevices, and this case is no exception.

Lei *et al.* (2012) developed a flexible capacitive pressure sensor for plantar (under the foot) applications. It consists of a PDMS dielectric layer, with electrodes for capacitance measuring attached, inside a flexible printed circuit film substrate.

A novel conductive gel-based pressure sensor was developed by Li *et al.* (2010). This gel is made of PDMS and, either carbon or metal particles. This sensor proved to be capable of measuring within the typical pressure range of most microfluidic devices. In line with other similar systems, it requires a dedicated fabrication process in order to be implemented.

In this thesis, the most practical solution for pressure drop measuring will be used, external pressure sensors. This is the simplest way for measuring pressure drops in existing PDMS microdevices with minimal modifications, hence being the most straightforward, repeatable and flexible method of all (Cheung *et al.*, 2012). In addition to only requiring the external sensors, with no design or extra

microfluidic device incorporation requirements, these can easily be coupled with high-speed data acquisition hardware, allowing for real-time dynamic measurements.

Materials and Methods

The measurement of fluid pressure in microchannels is difficult. No optimal solution exists regarding the design of pressure taps, nor guidelines concerning their shape, and its relation with the quality of the measurements. In an attempt to answer this need, an experimental study to evaluate the performance of different pressure tap configurations was devised. This study was quintessentially fundamental in nature, addressing only the flow of a Newtonian fluid inside plain straight microchannels. It comprised the following stages.

2.1 Microdevice design

The human body circulatory system is an intricate network of arteries, veins and capillaries, all of different shapes and sizes. This study will focus on the medium to small size (diameter < 1 mm) conduits of the human body. Straight 10 mm long rectangular microchannels, with a 270 μm across (L_h) and 100 μm in depth (L_v) cross-section, were designed, modelling a standard, yet simplified, blood vessel from the human circulatory system. The characteristic length-scale of the channels is therefore, $L_c = 135$ μm, half their side length. Each microchannel possesses its own inlet and outlet ports, followed by two built-in pressure taps (both 1.5 mm in diameter), one at the inlet and another one at the outlet of the straight channel, for additional pressure drop measurement purposes. Contraction-expansion sections were added where necessary, making for smooth transitions and hence avoiding any undesired disturbances in the flow caused by sudden cross-section area changes (see Figure 2.1).

Regarding the 2D microbot prototypes, their minimum length was set at 75 μm, ten times the average blood particle size, so that the hypothesis of continuous media would still be valid (Martínez-Aranda *et al.*, 2016). Two different geometries were considered for this study: a circular one and an elliptical one, with an aspect ratio of 1 : 4. The two shapes were chosen based on the work of Martínez-Aranda *et al.* (2016), who gathered the main features, morphology-wise, of several previously reported microbot prototypes and concluded on four general 3D models: a cube, a sphere and

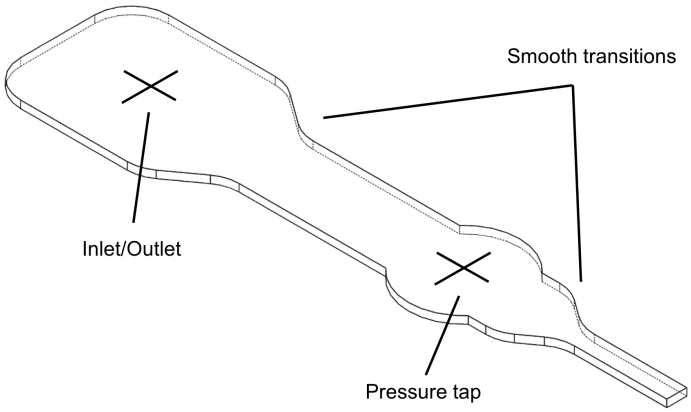

Figure 2.1: Smooth cross-section transition in the microchannels.

two different aspect ratio ellipsoids (1 : 2 and 1 : 4). In order to avoid the problem of blood particle interference, as explained before, the two prototypes considered in this study share the same characteristic length-scale $R_1 = 37.5$ µm. The characteristic length-scale R_1, represents half of the smallest dimension of these 2D geometries. Therefore, the diameter of the circular microbot and the minor axis of the elliptical one are both 75 µm. That results in a major axis of 300 µm for the elliptical prototype, attending its aspect ratio.

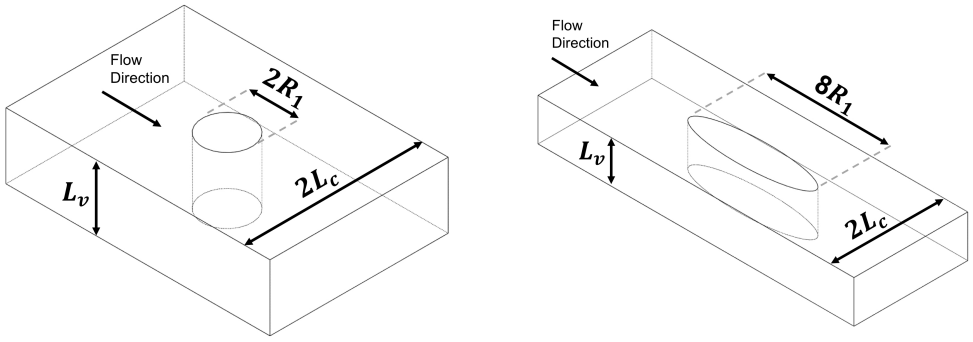

Figure 2.2: 2D microbot prototypes. Characteristic length-scale, R_1, is 37.5 µm. Aspect ratio of the elliptical model is 1 : 4.

The models stand streamwise oriented in the middle of the microchannels, equally distant from each wall to ensure the flow's even distribution around them. Note that, given the 2D nature of the problem, the microbot prototypes are actually pillars, stretching all the way from the channel's bottom to the top, with the desired outer shape. Enough space is left on either side to avoid severe wall effects, which are closely related to the blockage the flow undergoes in that section. This can be measured in terms of blockage ratio (β), here defined as the quotient between the prototype and the channel characteristic length-scales ($\beta = R_1/L_c \sim 0.28$). A β of ~0.28 means that approximately

28 % of the channel's cross-stream length is occupied by a microbot, blocking the flow's passage. The remaining ~72 % is what is left for the flow to run freely around the obstacle. 0.28 classifies as a low–moderate β, hence the influence of the channel walls on the model dynamics is not substantial. However, increasing the β to significantly higher values, say 0.5 for example, leads to more severe blockage effects, especially at low *Re* numbers (0.1–100) (Huang and Feng, 1995). Effects such as stronger pressure and friction drag, and increased viscous force at the model's surface intensify. Also, the narrowing of the gap between the obstacle and the inner walls contributes for a delay in boundary layer separation, only occurring at an angle further downstream on the prototype's surface, due to the stabilising influence of the channel walls, and resulting in wake size reduction. Moreover, the convective acceleration of the fluid in the gap leads to a greater pressure difference between the front and rear regions of the model (Huang and Feng, 1995, Krishnan and Kaman, 2010). That said, so as for the prototype dynamics not to be by any means compromised by excessive channel wall influence during the experiment, ensuring weak–moderate blockage conditions ($\beta < 0.3$), like the ones here achieved, is key.

The rectangular cross-section of the microchannels naturally gives rise to 3D flows. Minimising its influence on the experiment is therefore crucial in order to achieve valid results, true to the 2D conceptualisation of the problem. With that in mind and in order to accurately characterise the geometry of the device (so that comparisons to other experiments could be made), a confinement ratio that relates channel depth to microbot cross-stream length is introduced ($\Lambda = L_v/D \sim 1.3$). For both prototypes considered, $D = 75$ µm, two times their characteristic length-scale (R_1), since they are oriented towards flow direction.

A practical rule for avoiding entry effects and assuring fully developed flow in pipe flows is to consider a minimum entrance length of approximately ten times the cross-stream length, which in this case yields $L_e \sim 10\,L_h = 2.7$ mm. Attending to this basic principle, the microbot prototypes were placed ~2.9 mm away from the beginning of the straight channel, also ensuring that enough space was left for the flow to fully develop again, downstream of the models, therefore minimising the risk of exit effects taking place. The design of the microchannels was planned at the beginning also for the characterisation of complex fluid flows in the presence of different microbot prototypes. However, the complex and time consuming nature of the work, forced to limit the study to only a Newtonian fluid and channels with no prototypes inside.

In order to assess the pressure drop caused by the presence of the microbot, a couple of pressure taps, placed up and downstream and equally distant from its centroid, leading from the main flow channel were added. The taps are 500 µm away from the prototypes, on opposite sides, so that the pressure difference registered between the two is almost entirely due to their blockage (see Figure 2.3).

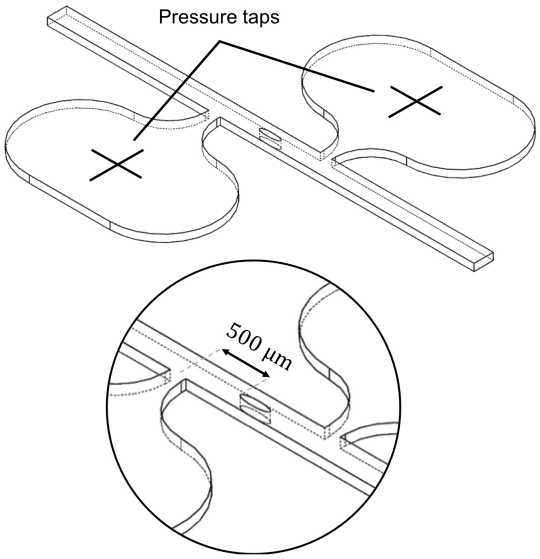

Figure 2.3: Design of the two main pressure taps in the microchannels.

Therefore, each microchannel has in total four different pressure taps, two far from the model, located at the inlet and outlet of the straight channel, and the other two immediately before and after the model (see Figure 2.4).

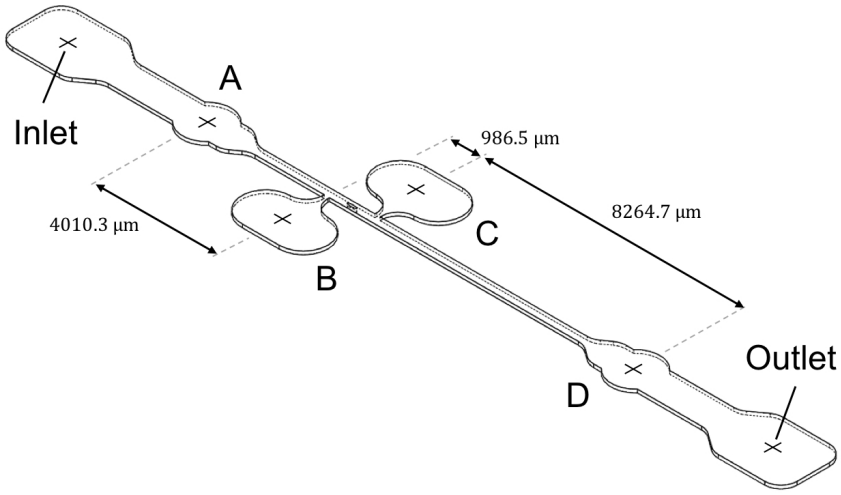

Figure 2.4: Distribution of the pressure taps along the microchannels.

The two pressure taps that sit close to the microbot do not have a built-in configuration like the other two. These, on the other hand, lead from the main flow channel through a narrower sub-channel that ultimately connects to a larger roundish area (~1.5 mm in diameter) in which the static pressure can be read. The configuration of these two taps will be subject of a parametric

study, in which several designs are tested in hopes of finding the best one overall. For that end, the different pressure tap shapes considered will be evaluated both qualitatively and quantitatively. That is, evaluation by experimental observation of their in-flow behaviour, such as the propensity for air bubble housing, and by pressure measurement results analysis and comparison to theoretical models.

A wide range of configurations was obtained by varying three key shape parameters: sub-channel width, w; tap cross-section transition radius of curvature, R; tap cross-section transition angle of inclination, α. The sub-channel's length was kept at a constant 50 µm for all configurations. For each shape parameter three representative values are considered, gradually increasing at a non-constant rate (different for each parameter) and arranged from smallest to largest according to numbers 1 to 3. The considered parameters and their respectively assigned values are shown in Table 2.1. The value of each parameter, representative of the design of the pressure taps, can be seen in Figure 2.5.

Table 2.1: Pressure tap shape parameters considered in the study and respectively assigned values

	w [µm]	R [µm]	α [deg]
1	54	50	15
2	108	250	45
3	162	500	75

A total of 18 different configurations can be arranged with these variables. Note that w can only combine with R and α individually, since these represent distinct forms of cross-section transitioning. In other words, solely one of the two parameters, R or α, can be employed in a pressure tap at a time. Besides the 18 plain microchannels used in this study, two other sets of these channels were designed, corresponding to the two microbot prototypes considered. Hence, the total number of microchannels designed was 54.

All microchannels were designed (Figure 2.6) in a computer-aided design program (CAD), Autodesk AutoCAD®, under the guidelines and layout constrains imposed by INESC MN - Microsystems and Nanotechnologies, where they would be later on materialised. The type of nomenclature used is explained in Tables 2.2 and 2.3.

By comparing the results obtained by the different pressure tap designs, the influence of the three shape parameters considered in the quality of the whole pressure measuring process can be assessed, qualitative and quantitative-wise. This way, an optimal tap configuration, within the sample range, can be ultimately proposed.

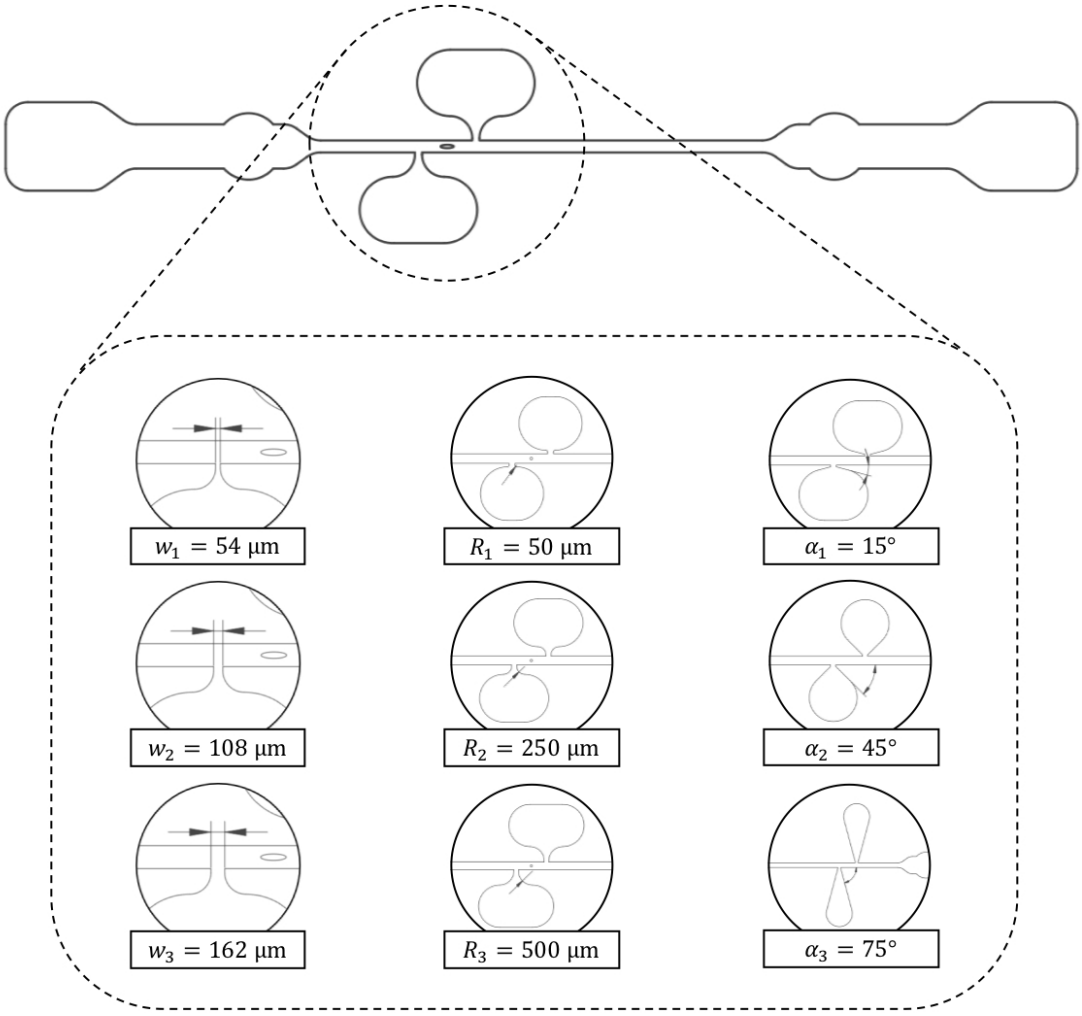

Figure 2.5: Different values for the representative parameters (w, R and α) of the pressure tap geometry.

2.2 Microdevice fabrication

From the conceptualisation and design of the microchannels to their materialisation, stands a two-stage fabrication process in between, whose details will now be presented.

The first stage of the process takes place at INESC MN's facilities. There, from the designs that had been developed, SU-8 molds of the microchannels were fabricated by order. To begin with, hard masks of the microchannels were created. These consist on aluminium (Al) coated (200 nm film) 10×10 cm Corning® glass substrates cut to size (25×75 mm and 50×75 mm pieces), in which the microchannels are cut out. With those, optical lithography (often referred to as photolithography) was used to create the channels' master molds on SU-8 coated 5×5 cm and 6×6 cm silicon substrates, that had been initially cut out from larger 6 inches silicon wafers. Examples of the molds can be seen in Figure 2.7. The resulting molds thickness (d), that corresponds to the microchannels depth (L_v),

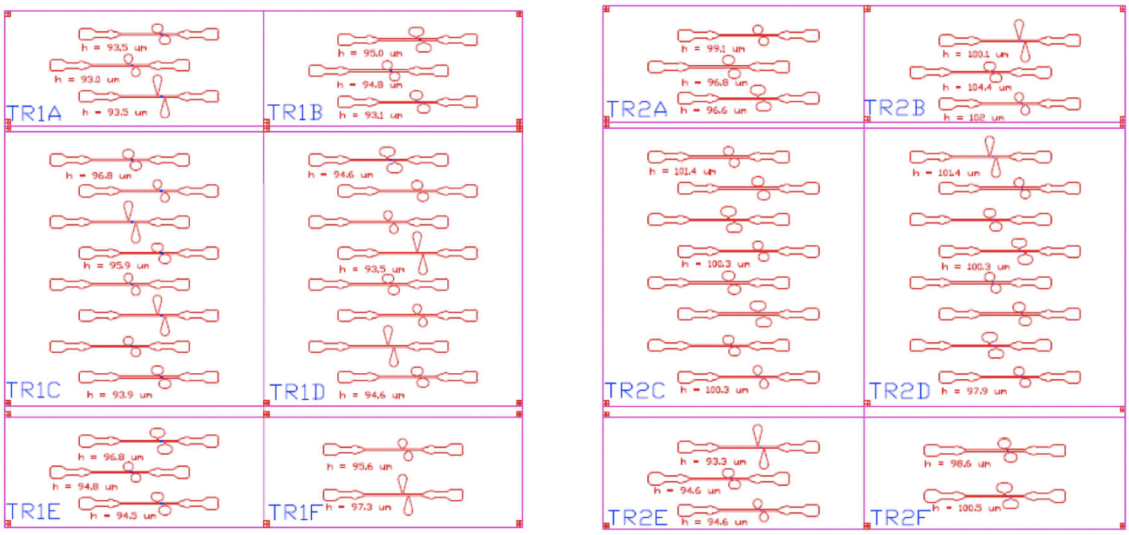

Figure 2.6: CAD designs of the 54 microchannels.

Table 2.2: Nomenclature for the designation of the microchannels from TR1 chips

	ref.	w	α	R	Microbot[(a)]	ref.	w	α	R	Microbot[(a)]
TR1	A1	1	1	–	E	B1	2	–	3	E
	A2	1	2	–	E	B2	3	–	1	E
	A3	1	3	–	E	B3	3	–	2	E
	C1	2	1	–	E	D1	3	–	3	E
	C2	2	2	–	E	D2	1	1	–	–
	C3	2	3	–	E	D3	1	2	–	–
	C4	3	1	–	E	D4	1	3	–	–
	C5	3	2	–	E	D5	2	1	–	–
	C6	3	3	–	E	D6	2	2	–	–
	C7	1	–	1	E	D7	2	3	–	–
	C8	1	–	2	E	D8	3	1	–	–
	E1	1	–	3	E	F1	3	2	–	–
	E2	2	–	1	E	F2	3	3	–	–
	E3	2	–	2	E					

[(a)]C = circular, E = elliptical.

presented variations of the order of ±10 µm around the 100 µm target. These errors will be taken into account later on for result analysis, since the specific thickness of some channels was provided

Table 2.3: Nomenclature for the designation of the microchannels from TR2 chips

	ref.	w	α	R	Microbot[(b)]	ref.	w	α	R	Microbot[(b)]
TR2	A1	1	–	1	–	B1	2	3	–	C
	A2	1	–	2	–	B2	3	1	–	C
	A3	1	–	3	–	B3	3	2	–	C
	C1	2	–	1	–	D1	3	3	–	C
	C2	2	–	2	–	D2	1	–	1	C
	C3	2	–	3	–	D3	1	–	2	C
	C4	3	–	1	–	D4	1	–	3	C
	C5	3	–	2	–	D5	2	–	1	C
	C6	3	–	3	–	D6	2	–	2	C
	C7	1	1	–	C	D7	2	–	3	C
	C8	1	2	–	C	D8	3	–	1	C
	E1	1	3	–	C	F1	3	–	2	C
	E2	2	1	–	C	F2	3	–	3	C
	E3	2	2	–	C					

[(b)]C = circular, E = elliptical.

(see Table 2.4 - for nomenclature please refer to Tables 2.2 and 2.3). Some minor defects in the molds were reported, but their experimental relevance is negligible.

The second stage of the fabrication process takes place at Faculdade de Engenharia da Universidade do Porto (FEUP). Here, standard soft-lithography, a simple technique based on replica molding and rapid prototyping (Xia and Whitesides, 1998, McDonald *et al.*, 2000, Ng *et al.*, 2002), was used for fabricating polydimethylsiloxane (PDMS) microchannels from their respective photo-resist (SU-8) molds.

Using etching techniques, silicon (or glass) based microchannels could also be fabricated with very good results, as seen in the works of Kohl *et al.* (2005b), Ateya *et al.* (2005) and Kuoni *et al.* (2003). But even though silicon is a great material for precise microfluidic device fabrication, it has its drawbacks: comes in at a high cost, the microfabrication process is time consuming and has some intricate steps along the way, and lacks optical transparency (opaque material). As an alternative, PDMS, a soft elastomer, is typically used. Its lower price and less time consuming channel fabrication process (while very similar in step structure) make it a much more reasonable choice for most applications in microfluidics. Moreover, it is transparent at optically visible wavelengths

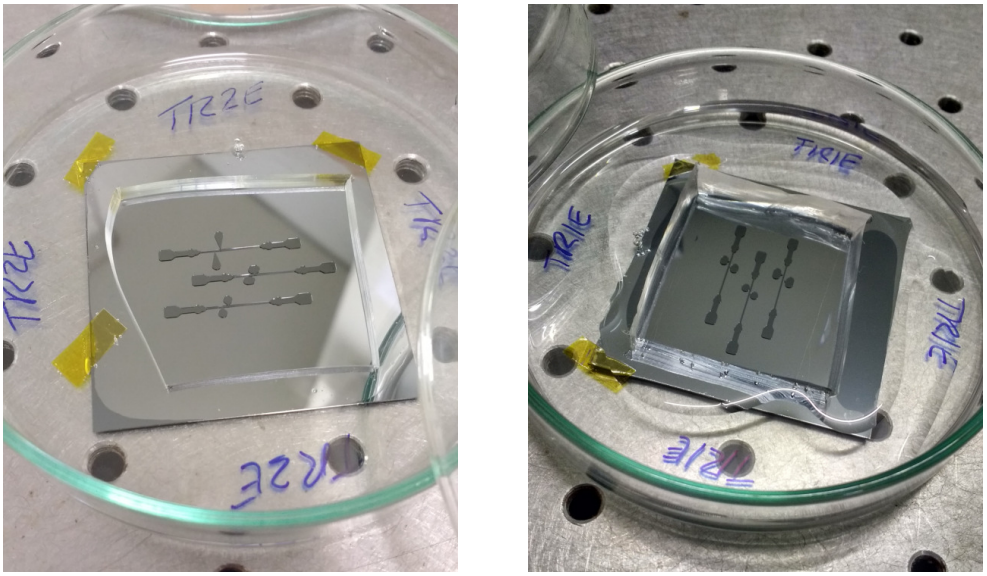

Figure 2.7: SU-8 master molds of the microchannels.

Table 2.4: SU-8 molds channel thickness, d: variations around a target depth, L_v, of 100 µm

	d [µm]			d [µm]	
ref.	TR1	TR2	ref.	TR1	TR2
A1	93.5	99.1	D1	94.6	101.4
A2	93.0	96.8	D4	93.5	100.3
A3	93.5	96.6	D8	94.6	97.9
B1	95.0	100.1	E1	96.8	93.3
B2	94.8	104.4	E2	94.8	94.6
B3	93.1	102	E3	94.5	94.6
C1	96.8	101.4	F1	95.6	98.6
C4	95.9	100.3	F2	97.3	100.5
C8	93.9	100.3			

(allowing the straightforward visualisation of the microchannels), biocompatible, deformable and has low autofluorescence. Such advantages over other materials, make this polymer a good candidate for manufacturing model vessels to study the blood flow dynamics (Unger *et al.*, 2000, Xia and Whitesides, 1998, Hardy *et al.*, 2009).

The PDMS channels were created using a two part Sylgard® 184 PDMS polymer kit (Dow Corning, Midland, MI, USA), mixed to a weight ratio of 10:1 (pre-polymer:cross-linker). Both components

were scaled carefully prior to mixing in order to make sure the 10 : 1 ratio was achieved. The two parts were mixed vigorously (∼5 min) and allowed to degas under vacuum in a desiccator for ∼1 h, so that the air bubbles introduced by the mixing could be removed. Because the silicon substrate of SU-8 molds is quite hydrophilic, and contact printing, between these and the PDMS mix, is the basis of soft-lithography, peeling problems when trying to demold the two parts will appear if the molds do not undergo any surface treatment to make them hydrophobic. This happens due to the PDMS's strong affinity to silicon, which causes it to stick to the SU-8 molds, since their surface contact angle is rather low (hydrophilic surface). Therefore, a silanization in gas surface treatment, with TMCS (TriMethylChloroSilane), was employed in order to turn the molds' surface hydrophobic (contact angle $> 90°$). The TMCS exposure lasted for ∼1 h and took place while the PDMS mixture was in the desiccator. Given the hazardous nature of this substance, the silanization was carried out under a fume hood for safety reasons. Once these tasks were completed, the PDMS mixture was poured over the silicon master molds, placed again under vacuum in the desiccator to remove any excess air bubbles, and then cured in an 80°C oven for half an hour. The PDMS was baked to accelerate the cross linkage process, which on its own, at room temperature, would take over 24 h to produce a solid enough result. At 80°C, a 30 min baking time frame is enough for achieving a soft PDMS consistency that allows for easy manipulation and piercing, once cooled down. When fully cured, the PDMS layers were gently cut, using a scalpel, and peeled off their molds. Next, the microchannels inlet, outlet and pressure sensing holes were made with a punch. Finally, the layers were bonded to PDMS spin coated 25×75 mm and 50×75 mm glass microscope slides, to close off the channels. Before bonding though, the PDMS coated slides were baked at 80°C for 20 min to make sure the thin coating was not runny, otherwise the two parts would slide when put together. The resulting PDMS chips were baked one last time, at 80°C for half an hour, and left to rest overnight, and only then were they ready for testing. The final result can be seen in Figure 2.8.

Using microscope imaging software, measurements of the PDMS channels width, w, were carried out in order to assess the degree of error (associated with this particular dimension) introduced by the whole device fabrication process. The chips selected for measuring were those with the plain microchannels (those that had no microbot model inside - see Tables 2.2 and2.3), since these would later be the object of the experiments. The chips were placed on the imaging stage of an inverted microscope (Leica Microsystems GmbH, DMI 5000 M) equipped with a sensitive monochromatic CCD camera (Leica Microsystems GmbH, DFC350 FX) and a 20× magnification objective lens (Leica HCX PL Fluotar L CORR, numerical aperture NA = 0.40). With these, the microscopy images were acquired and afterwards analysed using the Leica Application Suite software, or LAS (v3.5.0, Leica Microsystems), with which the real dimensions were measured. For each microchannel considered, three individual measurements were carried out at different locations (see Figure 2.9 for examples).

Figure 2.8: Microfabricated microfluidic chip.

The results are shown in Table 2.5 (note that the width was originally set at $L_h = 270$ µm for every channel) - for nomenclature please refer to Tables 2.2 and 2.3. Variations in the width dimensions with regards to the original value are due to the accumulated error of the SU-8 molds and PDMS chips fabrication processes. These will be later taken into consideration for result and error analysis.

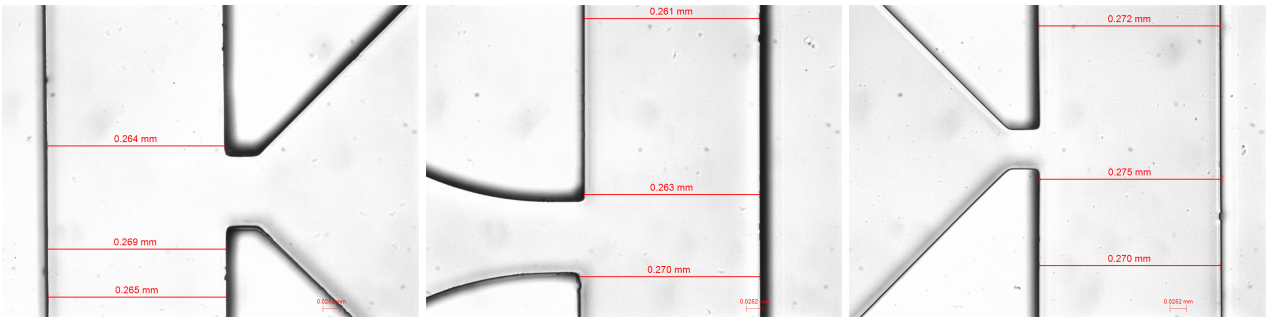

Figure 2.9: Microscope images of the microchannels for width, L_h, dimensional error analysis.

This concludes the two-stage microdevice fabrication process section. A detailed description of a similar protocol for PDMS channel fabrication can be found in Scott (2004). As expected, a clean and meticulous attitude towards each individual step of the process was adopted, avoiding grease and particle contamination as best as possible, not to compromise the end results.

Table 2.5: PDMS microchannels width, w: microscope imaging measurements (three for each microchannel) for posterior error analysis and comparison to the 270 µm (L_h) target

		w [µm]		
	ref.	#1	#2	#3
TR1	D1	272	267	264
	D2	262	267	261
	D3	270	264	266
	D4	282	276	271
	D5	276	271	268
	D6	264	269	265
	D7	272	266	264
	D8	267	271	264
	F1	269	276	–
	F2	271	265	–
TR2	A1	274	268	273
	A2	283	292	279
	A3	271	274	272
	C1	271	274	269
	C2	270	275	271
	C3	261	263	270
	C4	285	281	280
	C5	277	272	273
	C6	287	285	285
	C7	273	269	269
	C8	272	275	270

2.2.1 3D printed molds

3D printing has the potential to significantly change the field of microfluidics (Waheed *et al.*, 2016). Even though 3D printed structures, to this day, cannot compete with the resolution of those defined using photolithography, they do enable enhanced control of device geometries, including the profile of the channel cross-section and varying channel heights in a single microdevice (Hwang *et al.*, 2015). The number of 3D printed microfluidic devices has been rapidly growing over the years. Recently, several applications for 3D printing technology in organ-on-a-chip engineering have been reported

(Yi *et al.*, 2017, Chen *et al.*, 2017). The substitution of photo-resist (SU-8) molds by 3D printed ones, for PDMS microchannel fabrication, has already been tried with interesting results (Hwang *et al.*, 2015). Despite not matching the resolution and surface smoothness standards of the conventional approach, results obtained from 3D printed molds were not discouraging.

3D printed molds of the microchannels were fabricated, in order to assess the actual degree of resolution of this technology and wether it could be used for further manufacturing of the intended geometries, or not. To fabricate these molds, two stereolithography (SL) printers were used, a standard one and another that uses digital light projection (DLP). In SL, a 3D object is built layer-by-layer by using selective light exposure to photo-polymerise a liquid resin. With DLP printers, higher resolution pieces can be produced, since here the minimum feature size is determined by the size of a projected pixel, whereas for conventional SL printers it depends on the laser spot size and absorption spectra of the photoresins (Bhattacharjee *et al.*, 2016).

The standard SL printer used (Formlabs® Form2) has an X : Y resolution of 150 µm (it has a laser spot size of 140 µm). The SL-based DLP printer (Creative CADworks® MiiCraft µMicrofluidics Edition) is capable of achieving an X : Y resolution of up to 30 µm, much in line with the above mentioned. MiiCraft machines have been used by several research groups (Waheed *et al.*, 2016). Three sample microchannels were selected for printing. The resulting molds are shown in Figure 2.10.

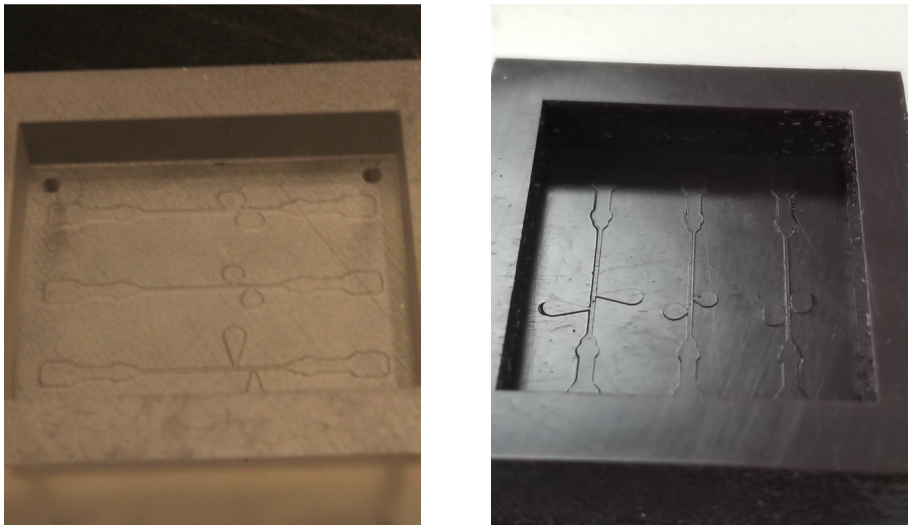

Figure 2.10: 3D printed molds for microfluidic device fabrication, manufactured by conventional stereolithography, SL (left), and SL with digital light projection, DLP (right).

At naked eye the overall surface roughness of the conventional SL molds looked smooth. PDMS layers were fabricated with these and tryout chips were made. A flow of fluorescent tracer particles was introduced in order to draw some conclusions. Microscope observations helped to conclude

that the layer interface inherent to the layer deposition process, characteristic of this fabrication technique and barely distinguishable at first, provokes clear distortion of the microchannels (as seen in Figure 2.11). This is naturally due to the machine's resolution.

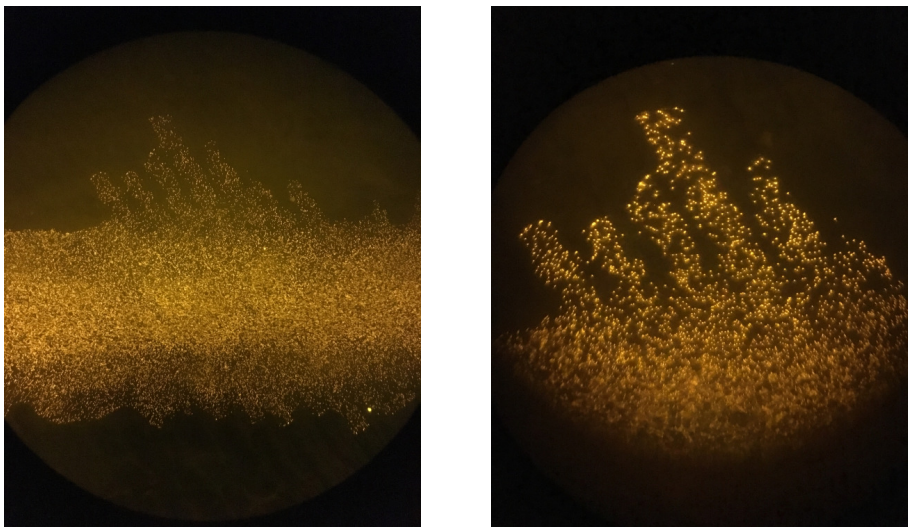

Figure 2.11: Defects observed in polydimethylsiloxane (PDMS) microchannels fabricated with standard stereolithography (SL) 3D printed molds.

Regarding the SL-DLP 3D printed molds, the level of detail achieved is clearly higher, when compared with the previous ones. The microbot prototypes clearly stand out and the walls of the channels seem vertical.

2.3 Pressure drop measurements

Attending to the preliminary character of this work, with the intention of further enriching it in the future by addressing the complex nature of blood flow in the human circulatory system (thus contemplating viscoelastic fluids), the tests were carried out with a Newtonian fluid, de-ionised (DI) water, as a controlled experiment. This way results could be plotted against conventional Newtonian models for validation, whilst giving an insight on which pressure tap configurations perform the best, and also compared to those of non-Newtonian fluids in future works.

The Reynolds number characterising the flow inside the microchannels is defined as $Re_c = \rho U_m D_h / \mu$, where ρ is the working fluid's density, μ is its constant viscosity, U_m is the mean velocity in the channel and $D_h = 2L_h L_v / (L_h + L_v)$ is its hydraulic diameter. The flow rates, Q, considered ranged from 0.0185 µl s^{-1} to 18.5 µl s^{-1}, leading to a Re_c interval from ~0.1 up to ~100 (characteristic of the flow regime in the human body circulatory system at small–medium blood vessels (Berger

et al., 1996)). Regarding the transition from laminar to turbulent flow, a collection of data on critical Reynolds numbers in microchannels of rectangular cross-section can be found in Hetsroni *et al.* (2005). It shows that transition to turbulence occurs for $Re_{cr} \geq 200$, whether it is in smooth or rough channels, hence the flow regimens here considered are strictly laminar. The mean velocities $U_m = Q/A_T$ in the microchannels were 0.686 mm $s^{-1} \leq U_m \leq 686$ mm s^{-1}, where A_T refers to the channels cross-section area.

The pressure drop (ΔP) at different flow rates (Q) was measured using Silicon Microstructures, Inc. SM5852 Series piezoresistive differential pressure sensors (SM5852-015W, SM5852-001 and SM5852-003), with a response time of 2 ms, which can cover a differential pressure range of ±2.1 kPa. The individual pressure ranges of sensors SM5852-015W, SM5852-001 and SM5852-003 are 0–0.05 PSI (0.373 kPa), 0–0.15 PSI (1 kPa) and 0–0.3 PSI (2.1 kPa), with an accuracy of 5.595×10^{-3} kPa, 0.02 kPa and 2.1 kPa, respectively. Depending on the fluids and flow rates tested, each pressure sensor was employed when best suited for the expected pressure drops. A 5 V DC power supply (Elektro-Automatik, PS 5200-02 A) was used to power the pressure sensors, which were also connected to a computer via a NI USB-6218 Series data acquisition (DAQ) card (National Instruments, Austin, TX) - all connections were made on a solder-less breadboard - in order to record the output data, at an acquisition rate of 1000 Hz, using a custom built program written in LabVIEW v8.2.1 (whose interface can be seen in Figure 2.12).

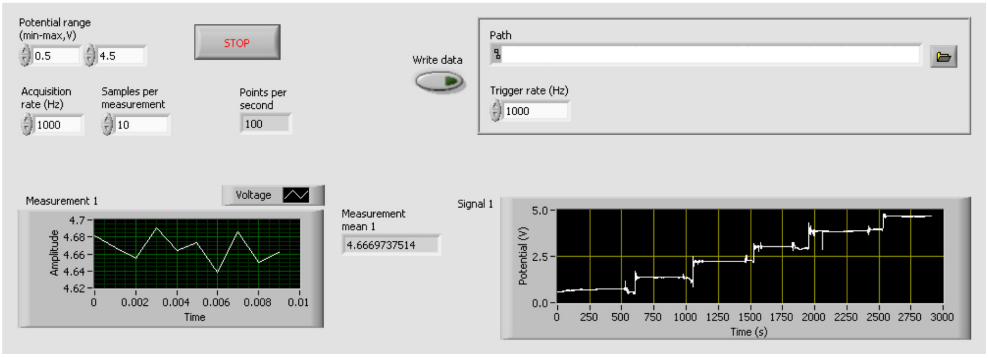

Figure 2.12: LabVIEW data acquisition software interface.

The transient response of the pressure sensors was continuously recorded until a steady-state condition (i.e., steady flow) was achieved, that is once the pressure drop readings ceased to change with time (in other words, when the voltage signal levelled off). Such state is characterised by a plateau with superimposed low amplitude oscillations, mostly caused by electronic noise. Steady-state pressure drop was typically achieved within 30–90 s with the DI water. From that point, the pressure data was sampled at a rate of 10 Hz for never less than 60 s (this was always at least 600 data points). An arithmetic averaging method was performed over the collected data.

The connections between the transducers ports and the microchannels pressure taps were established via flexible Tygon® tubing and Nordson Corporation stainless steel precision dispensing tips with an inner diameter (i.d.) of 0.008 inch (0.2032 mm) - see Figure 2.13. In order to avoid excessively long transients in the pressure drop upon changing the flow rate, the length of this flexible tubing should be reduced as much as possible (Adzima and Velankar, 2006). This time delay, between specifying the flow rate and the pressure reaching its steady-state value, has been previously observed in experimental pressure measurements with both Newtonian and non-Newtonian fluids (Scott, 2004, Yesilata *et al.*, 2000), each displaying a different behaviour. Whereas with a Newtonian fluid increasing the flow rate decreases the transient response period, the viscosity of a viscoelastic fluid causes it to behave in precisely the opposite way, thus increasing it with flow rate (Yesilata *et al.*, 2000). These transients are likely to be caused by air compressibility and component compliance effects. As the pressure sensors take data, the working fluids are not directly touching the sensors die (or membrane). Instead, air is trapped in the pressure tubing between these. Therefore, the pressure reading is equivalent to the pressure undergone by the air, since this one is compressed to equal the pressure in the taps. Along with the compression a pressure gradient is generated, leading to believe that the amount of time required for the liquid to compress the air to steady state is partially responsible for the sensors transient response. The elasticity of the various components of the setup also impacts this lag. Due to the deformability of the tubing and the PDMS, these expand under pressure, receding later to an undeformed state as steady-state is reached. Despite the air compressibility effects, which are inevitable, the use of shorter tubing helps to minimise transient response times, as mentioned. All things considered, the resolution of the dynamic pressure measurements was limited by the sampling rate of the DAQ card, response time of the pressure sensors, and signal-noise from vibrations and flexing of elastic components.

The pressure sensors were previously calibrated using two scaled static columns of water (at 20°C and with a corresponding density, ρ, of 998.2 kg/m^3), in which pressure differences were created by the injection/removal of liquid with plastic syringes that controlled each hydrostatic head. Therefore, the calibration curves were obtained by applying known hydrostatic height differences ($\Delta P = \rho g \Delta H$, where g is the gravity, and ΔH is the height difference of the columns) to both ends of the pressure transducers and measuring the resulting voltage outputs, correlating the two afterwards. Because the transducers sensing membranes are not meant to be in direct contact with liquids, under the risk of tearing, extra tubing was added between the sensors and the water columns, serving as an intermediate medium (air) for pressure transmission. A simple hydrostatic analysis shows that the tubes have to be of equal length for the pressure difference in the water to match the one measured by the sensors. Even though a steady-state regime was easier to achieve whilst calibrating, with almost no transient response registered given the hydrostatics involved, these tubes were

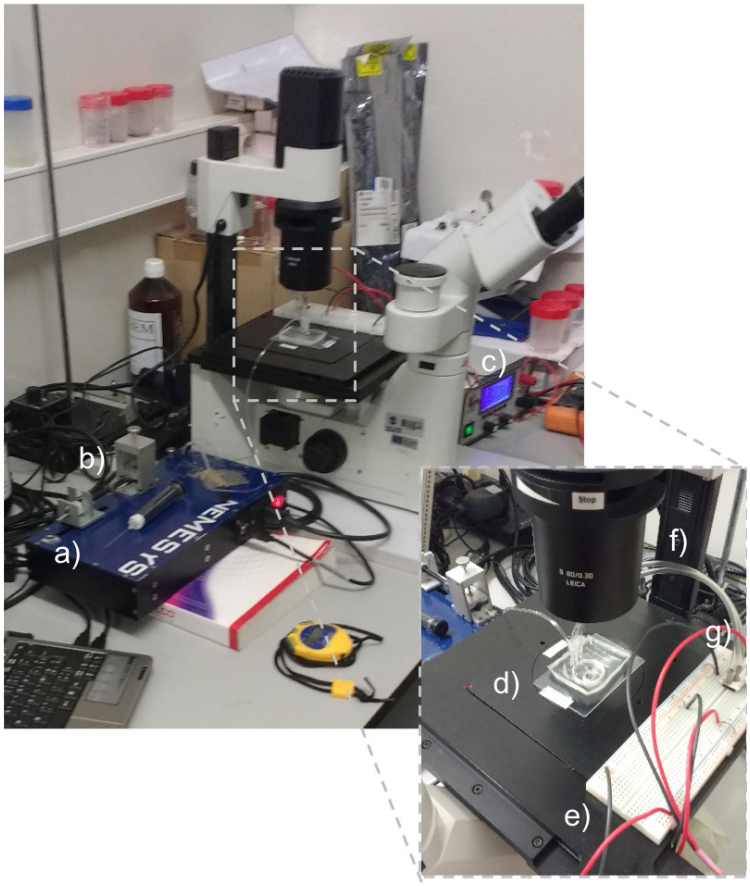

Figure 2.13: Experimental setup for pressure drop measuring in microchannels: a) low pressure syringe pump; b) glass syringe; c) power supply; d) microfluidic chip; e) signal cables; f) air-filled pressure sensing tubes; g) external pressure sensor.

kept short, in order to minimise the above mentioned effects of tubing elasticity and vibration. The connection between each column, plastic syringe and air-filled tube was assured by a three-way microfluidic valve. The results of the linear regression analysis of the calibration data for each pressure sensor, thus the calibration curves slope and y-intercept ($\Delta P = mV + b$), are shown in Table 2.6. The calibration curves were later used to relate the measured voltage output to a differential pressure drop measurement, at different applied flow rates in the microchannels (these are shown in Figures 2.14–2.16).

The flow rate was controlled using a neMESYS low pressure syringe pump (Cetoni GmbH). The pump operates on a stepper motor that pushes the syringe's shaft at a constant speed (Scott, 2004). Thus to ensure that the time interval between steps on the motor is small enough not to impact the flow rate in the channels, a minimum pusher velocity must be set (hence a minimum flow rate for each syringe), below which pulsating effects might occur. Therefore, depending on the required flow rate, different glass syringes (Hamilton® 2.5 ml and 10 ml volume) were used, ensuring pulsation-

Table 2.6: Slope, m, and y-intercept, b, of the calibration curves for the differential pressure sensors

Series	ref.	m (slope)	b (y-intercept)
SM5852	015W	181.02	−441.93
	001	256.18	−123.58
	003	509.78	−299.48

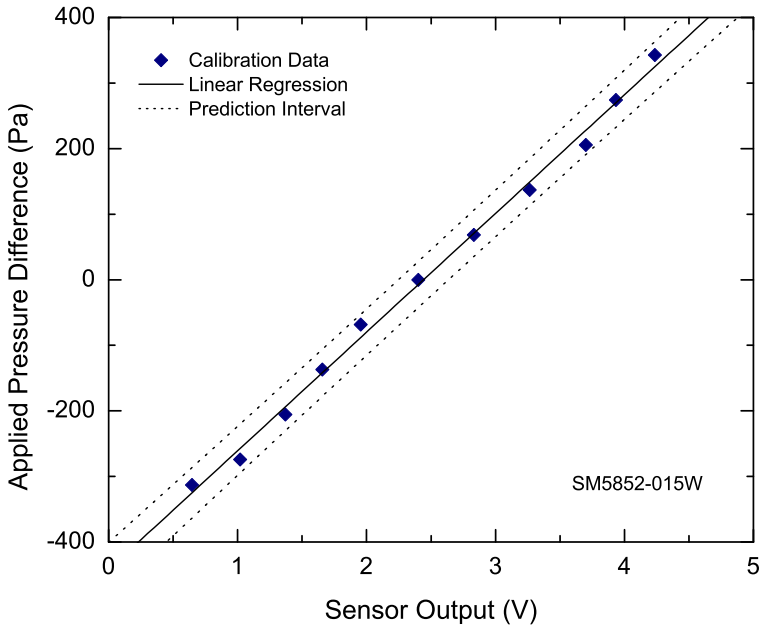

Figure 2.14: Calibration curve for pressure sensor SM5852-015W.

free dosing. These were connected to the microgeometries via Tygon® tubing of 0.44 mm i.d. and a precision dispensing tip with 0.008 inch (0.2032 mm) i.d. (Nordson Corporation). The pump controlled the channels inlet flow rate, while the outlet was left open to the atmosphere to balance the flow. Several alternative methods for developing flow within microfluidic channels have been reported, from electrophoresis techniques to the stimulation of osmotic movements, although none capable of achieving flow velocities >1 mm/s (Scott, 2004).

Since each microchannel has four pressure measuring zones, a built-in pressure tap in each end and two leading from the main flow channel (located closer to its middle, where the microbot sits), pressure drops at different flow rates were measured across four individual stretches along the channels - AB, BC, CD and AD (see Figure 2.4). The distance between pressure taps, L, can be seen in

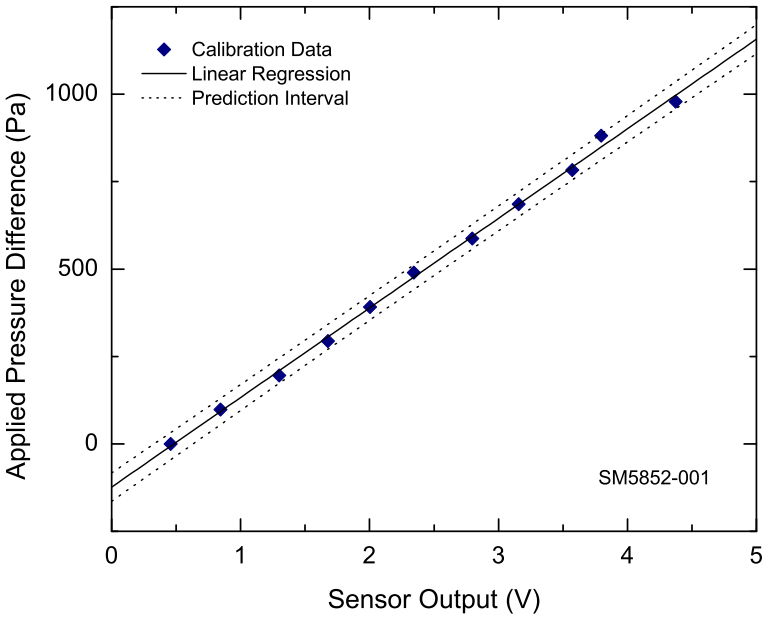

Figure 2.15: Calibration curve for pressure sensor SM5852-001.

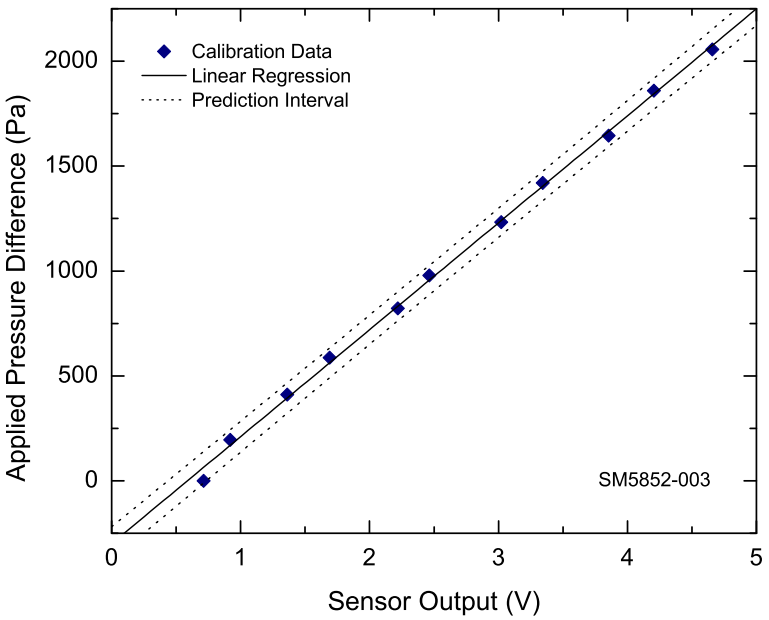

Figure 2.16: Calibration curve for pressure sensor SM5852-003.

Table 2.7. For each distance it is expected the pressure drop to be different, according to basic horizontal pipe flow theory - flow is governed by a balance between viscous and pressure forces in which pressure drop is directly proportional to pipe length (Munson *et al.*, 2013). Hence, a relation like so $\Delta P_{BC} < \Delta P_{AB} < \Delta P_{CD} < \Delta P_{AD}$ should be obtained for each microchannel. All the experiments were carried out at a controlled room temperature of ~20°C.

Table 2.7: Distance between pressure taps, L, across which pressure drop measurements, ΔP, were carried out, according to Figure 2.4

Stretch	L [µm]
AB	4010.3
BC	986.5
CD	8264.7
AD	13261.5

Results and Discussion

3.1 Uncertainty analysis

A careful analysis of the experimental uncertainty in this study is critical to the interpretation of the experimental data and exploration of deviations from the theory. Experimental uncertainties were estimated for pressure drop, ΔP_{exp}, and Reynolds number, Re. The uncertainties in the analytical model were estimated as well, ΔP_{theor}. Starting with the experimental pressure drop, ΔP_{exp}, the absolute uncertainty in it is given by:

$$U_{\Delta P_{\text{exp}}} = \left(B_{\Delta P_{\text{exp}}}^2 + P_{\Delta P_{\text{exp}}}^2 \right)^{\frac{1}{2}} , \tag{3.1}$$

with $B_{\Delta P_{\text{exp}}}$ being the systematic error and $P_{\Delta P_{\text{exp}}}$ the random error.

The systematic error, $B_{\Delta P_{\text{exp}}}$, is entirely caused by instrumentation, namely the DAQ card and pressure sensors. This error is given by:

$$B_{\Delta P_{\text{exp}}} = \left(B_{\text{aq}}^2 + B_{\text{A/D}}^2 + B_{\text{sens}}^2 \right)^{\frac{1}{2}} , \tag{3.2}$$

with B_{aq} being the systematic errors related to the DAQ's signal acquisition, $B_{\text{A/D}}$ the systematic errors related to the DAQ's analog–digital conversion (A/D), and B_{sens} the systematic errors related to the pressure sensors.

Regarding the DAQ card, both the B_{aq} and $B_{\text{A/D}}$ errors are shown in Table 3.1. The resolution in microvolts is determined according to the formula:

$$\text{Resolution [V]} = \frac{\text{Range [V]}}{2^{\text{Resolution [bits]}}} . \tag{3.3}$$

B_{aq} corresponds to the DAQ's accuracy at full-scale (FS), which is specified by the supplier.

The systematic errors related to the pressure sensors, B_{sens}, were determined as shown in Table 3.2.

Table 3.1: Systematic errors related to the DAQ's signal acquisition and analog–digital conversion (A/D)

Series	Resolution [bits]	Range [V]	Resolution [μV]	$B_{A/D}$ [μV]	B_{aq} [μV][(a)]
NI USB-6218	16	0–5	76.29	38.15	1410

[(a)]Specifications from the supplier.

Table 3.2: Systematic errors related to the pressure sensors

Series	Model	FS range [kPa][(b)]	Accuracy [% FS][(b)(c)]	B_{sens} [Pa]
SM5852	015W	0.3730	1.5	5.59
	001	1	2	20.00
	003	2.1	1.6	33.60

[(b)]FS = full-scale.

[(c)]Specifications from the supplier.

The systematic error in the experimental pressure drop, $B_{\Delta P_{exp}}$, can now be determined with Equation 3.2, for each pressure sensor. The results are shown in Table 3.3. The DAQ's signal acquisition and analog–digital conversion (A/D) errors are the ones presented in Table 3.1, having the change of units been made resorting to the pressure sensors sensibility. The sensibility is computed as follows:

$$\text{Sensitivity} = \frac{\text{FS output}}{\text{FS range}} . \tag{3.4}$$

Table 3.3: Systematic error in the experimental pressure drop

Series	Model	FS output [V][(d)]	Sensitivity [μV/Pa]	B_{sens} [Pa]	$B_{A/D}$ [Pa]	B_{aq} [Pa][(e)]	$B_{\Delta P_{exp}}$ [Pa]
SM5852	015W	4.5	12065.6	5.59	0.003	0.117	5.596
	001	4.5	4500.0	20.00	0.008	0.313	20.002
	003	4.5	2142.9	33.66	0.018	0.658	33.606

[(d)]FS = full-scale.

[(e)]Specifications from the supplier.

The random error in the experimental pressure drop, $P_{\Delta P_{exp}}$, is related with the randomness in the sampled voltage readings for each flow rate tested and with the linear regression used to obtain

the calibration curves for each pressure sensor. This error is given by:

$$P_{\Delta P_{\text{exp}}} = \left(P_{\overline{V}}^2 + P_{\text{lin}}^2 \right)^{\frac{1}{2}} , \tag{3.5}$$

with $P_{\overline{V}}$ being the uncertainty in the average value of the sampled voltage readings for each flow rate tested and P_{lin} the error in the linear fit of the calibration data for each pressure sensor.

Regarding $P_{\overline{V}}$, it is determined by the expression:

$$P_{\overline{V}} = \frac{t\, S_V}{\sqrt{N}} , \tag{3.6}$$

where t is the Student's t-distribution parameter for a 95 % confidence interval, S_V is the standard deviation of the sampled readings and N is the total number of readings. Since the number of readings is high (never less than 600 data points), $t \sim 2$ was considered (Coleman and Steele, 2009). This uncertainty was computed for each measurement.

The error in the linear fit of the calibration data, P_{lin} (related with the linear regression), is given for each pressure sensor by the expression:

$$P_{\text{lin}} = 2 \left[\frac{\sum_{i=1}^{N} (y_i - m x_i - c)^2}{N - 2} \right]^{\frac{1}{2}} . \tag{3.7}$$

These are shown in Table 3.4 (Coleman and Steele, 2009).

Table 3.4: Errors related to the linear regression analysis of the calibration data from each sensor

Series	Model	P_{lin} [Pa]
SM5852	015W	29.78
	001	29.81
	003	58.69

The uncertainty associated with the Reynolds number, Re, is based on the actual dimensions of the microchannels cross-section, w (width) and d (depth). These are shown in Tables 2.5 and 2.4, respectively. For simplification, only the errors in w and d were considered, thus neglecting those from the other variables. Re can be expressed as a function of w and d as follows:

$$Re = \frac{2\rho Q}{\mu\,(w + d)} . \tag{3.8}$$

The uncertainty can be estimated using:

$$\delta Re = \left[\cancel{\left(\frac{\partial Re}{\partial \rho} \delta \rho \right)^2} + \cancel{\left(\frac{\partial Re}{\partial Q} \delta Q \right)^2} + \cancel{\left(\frac{\partial Re}{\partial \mu} \delta \mu \right)^2} + \left(\frac{\partial Re}{\partial w} \delta w \right)^2 + \left(\frac{\partial Re}{\partial d} \delta d \right)^2 \right]^{\frac{1}{2}}, \tag{3.9}$$

which yields:

$$\delta Re = \frac{2\rho Q}{\mu (w+d)^2} \sqrt{\left(\delta w^2 + \delta d^2 \right)}, \tag{3.10}$$

where δw and δd are the uncertainties in the average values of the widths and depths, respectively, measured in the actual microchannels, $P_{\overline{w}}$ and $P_{\overline{d}}$. So, both are determined in similar fashion as $P_{\overline{V}}$ (see Equation 3.6). Although now, because of the low number of measurements taken for each channel, in the case of w, and for each chip, in the case of d, t is that of the Student's t-distribution.

The uncertainties in the theoretical model, ΔP_{theor}, are estimated in the same way as for the Reynolds number, since the only sources of error considered are too, w and d. The calculation sequence, starting with the model's expression at Equation 3.16, is now presented:

$$\delta \Delta P_{\text{theor}} = \left[\cancel{\left(\frac{\partial \Delta P_{\text{theor}}}{\partial L} \delta L \right)^2} + \cancel{\left(\frac{\partial \Delta P_{\text{theor}}}{\partial Q} \delta Q \right)^2} + \cancel{\left(\frac{\partial \Delta P_{\text{theor}}}{\partial \mu} \delta \mu \right)^2} + \left(\frac{\partial \Delta P_{\text{theor}}}{\partial w} \delta w \right)^2 + \left(\frac{\partial \Delta P_{\text{theor}}}{\partial d} \delta d \right)^2 \right]^{\frac{1}{2}}, \tag{3.11}$$

$$\delta \Delta P_{\text{theor}} = \frac{12 L Q \mu}{w d^2} \left[\frac{\delta w^2}{w^2} \left(-\frac{1}{w} - \frac{\left(1 + \frac{d}{w}\right)}{d} \right)^2 + \frac{\delta d^2}{d^2} \left(\frac{1}{w} - \frac{3\left(1 + \frac{d}{w}\right)}{d} \right)^2 \right]^{\frac{1}{2}}. \tag{3.12}$$

Attending that $\Delta P/L$ was plotted, and not ΔP, the uncertainties in both the experimental and theoretical pressure drops per unit length (the latter one given by the analytical model) need to be determined. However, since no errors were considered for the distances between taps, L, these uncertainties are given by:

$$U_{\left(\Delta P_{\text{exp}}/L\right)} = \frac{U_{\Delta P_{\text{exp}}}}{L}, \tag{3.13}$$

$$U_{\left(\Delta P_{\text{theor}}/L\right)} = \frac{U_{\Delta P_{\text{theor}}}}{L}. \tag{3.14}$$

3.2 Results analysis

In this Section the experimental results are presented and discussed. Figures 3.1–3.3 show the steady state pressure drop per unit length ($\Delta P/L$) versus Reynolds number (Re) for DI water in the microchannels with pressure tap sub-channel width w_1, w_2 and w_3, respectively. Pressure drop per unit length was plotted to discard the influence of the distance between taps in the results, thus expecting that the pressure drops measured in stretches AB, BC, CD and AD would all fall in the

same $\Delta P/L$, for each of the Reynolds numbers considered. This way, it should be easier to draw conclusions from the plotted data.

In each figure, the experimental data is plotted against its correspondent theoretically predicted curve, shown by a solid line. Analytical models for pressure drop in a capillary are based on conventional laminar flow theory (White, 2006), according to which for fully developed flow in a straight rectilinear channel of known dimensions the pressure drop is given by the force balance $wd\Delta P = 2L(w + d)\tau$, where L is the channel length, w and d are, respectively, the channel cross-section width and depth, and τ is wall shear stress. From this balance yields $\Delta P = 2\tau L(w + d)/wd \sim 2\tau L/d$, thus showing the influence of channel aspect ratio, w/d, on the pressure drop - when $L/d \gg 1$ and $w/d \gg 1$ the resulting pressure drops can be very large. These models consist on reliable approximate solutions to the Navier-Stokes equation (typically within 10 % error) that are much simpler than the considerably more intricate Hagen-Poiseuille exact formula for pressure drop in rectangular channels (White, 2006).

The theoretical model here considered is for a rigid rectangular channel cross-section and assumes fully developed, steady state, laminar Newtonian flow (Pipe and McKinley, 2009). It is expressed as

$$\frac{\Delta P_{\text{theor}}}{L} = \frac{2kQ\left(1 + \frac{d}{w}\right)\mu}{wd^3}, \tag{3.15}$$

with Q being the flow rate, μ the dynamic viscosity and k a numerical factor depending on the channel geometry: $k = 6$ for a slit channel ($w/d \gg 1$) and $k = 14.3$ for a square channel ($w/d = 1$). The original cross-section width and depth for the microchannels in this work are $L_h = 270$ µm and $L_v = 100$ µm, respectively. According to the model's nomenclature this results in an aspect ratio of $w/d = L_h/L_v = 2.7 \gg 1$ and thus, $k = 6$:

$$\frac{\Delta P_{\text{theor}}}{L} = \frac{12Q\left(1 + \frac{d}{w}\right)\mu}{wd^3}. \tag{3.16}$$

A similar analytical model for pressure drop in a capillary, whose results show great resemblance with the ones computed using the model above can be found in Cheung *et al.* (2012).

The pressure drop per unit length was expected to increase linearly with Reynolds number, as required by conventional laminar flow theory. Indeed, in each channel the pressure drops per unit length were found to be approximately linear with Reynolds number (see Figures 3.1–3.3). Some minor non-linearity might have been caused by the compliance of the PDMS walls: as pressure increases, the walls flex slightly, thus increasing the inner dimensions of the channel. And by consequence, changes in the microchannels cross-sectional area lead to changes in pressure drop as well. Note that the analytical model used (Equation 3.16) assumes rigid channel cross-section, thus not contemplating the elastic nature of PDMS and the possibility of cross-sectional deformation. Some

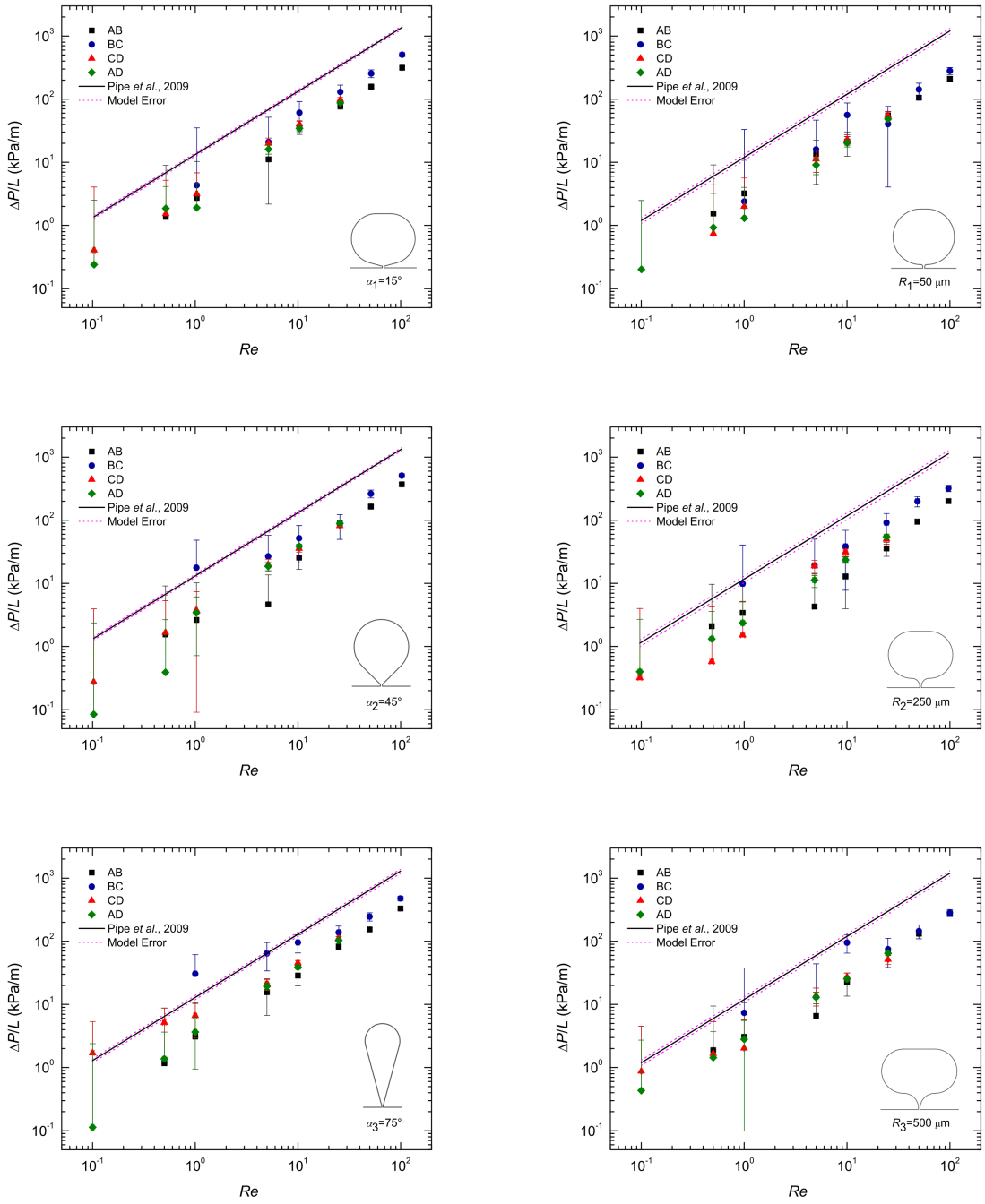

Figure 3.1: Steady state pressure drop per unit length ($\Delta P/L$) versus Reynolds number (Re) for DI water. Pressure tap sub-channel width $w_1 = 54$ μm. Pressure taps varying α (left column) and varying R (right column) in their design.

works have discussed the importance of bulk deformation in rectangular microchannels. Gervais *et al.* (2006) studied the elastic deformation of PDMS microchannels under imposed flow rates. Fol-

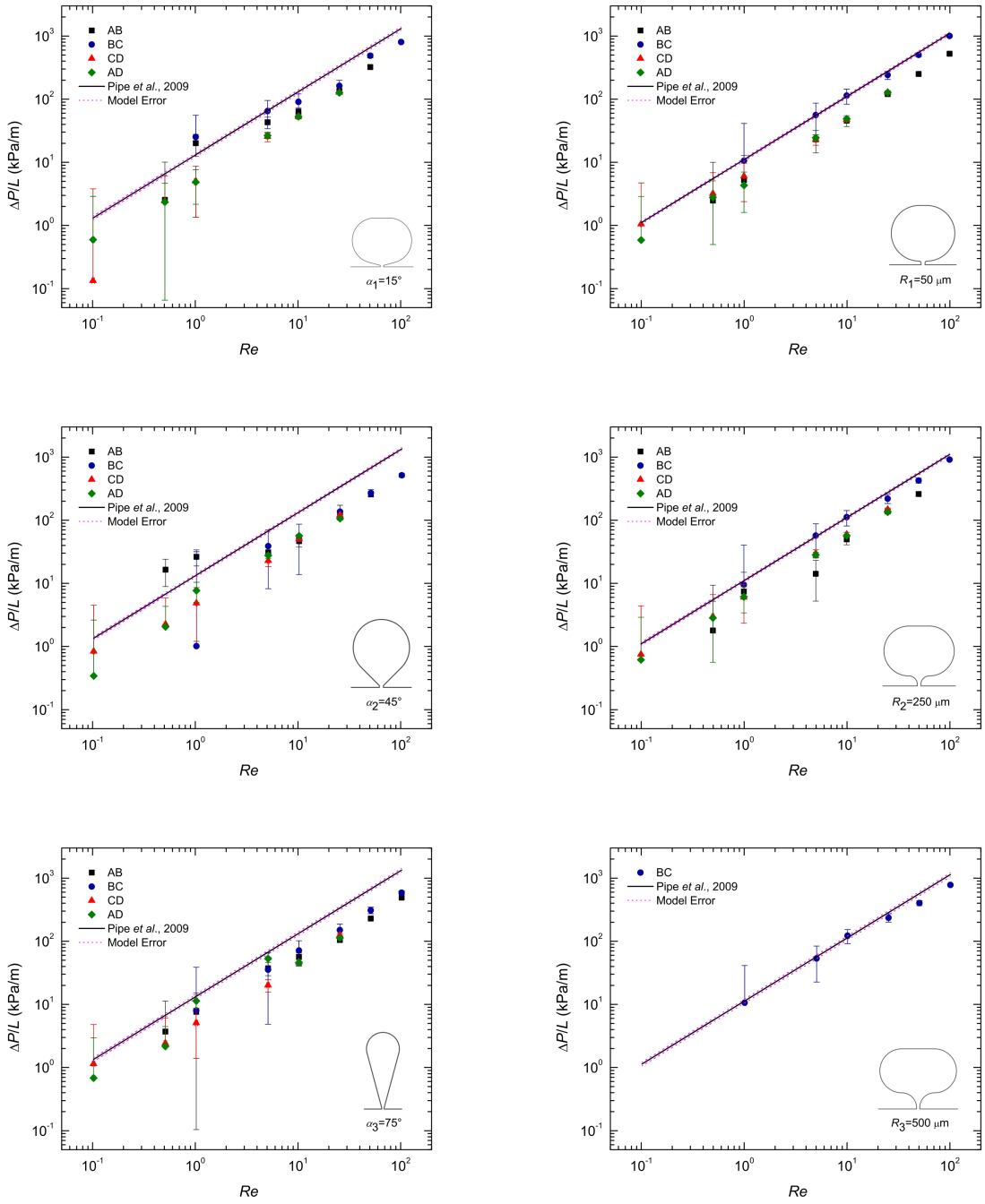

Figure 3.2: Steady state pressure drop per unit length ($\Delta P/L$) versus Reynolds number (Re) for DI water. Pressure tap sub-channel width $w_2 = 108$ μm. Pressure taps varying α (left column) and varying R (right column) in their design. The lack of pressure data in the bottom right plot was caused by leakage problems.

lowing up on this study, Cheung *et al.* (2012) developed an elastic rectangular expression capable of predicting pressure drop in deformable PDMS microchannels. Results obtained by Gervais *et al.*

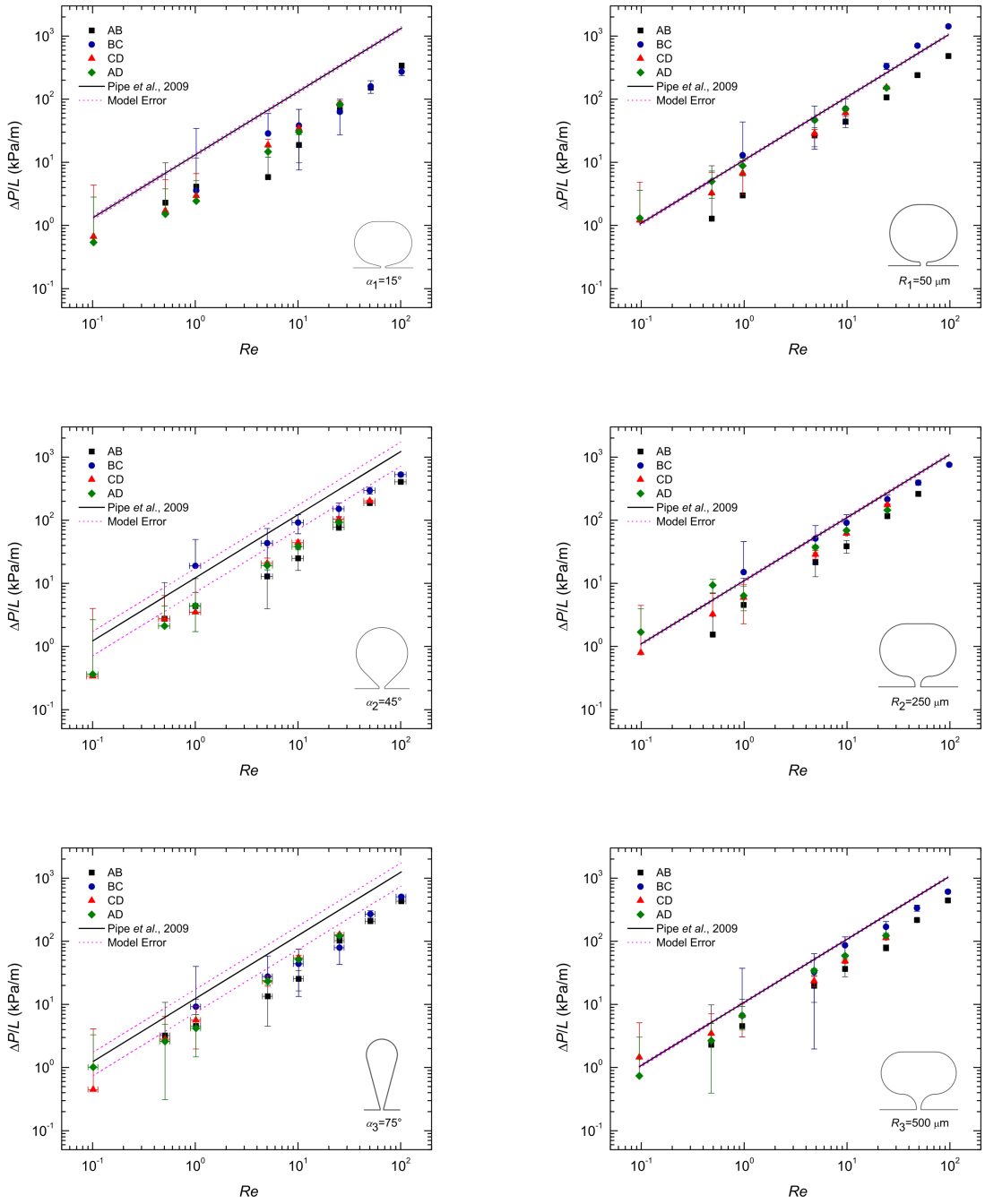

Figure 3.3: Steady state pressure drop per unit length ($\Delta P/L$) versus Reynolds number (Re) for DI water. Pressure tap sub-channel width $w_3 = 162$ μm. Pressure taps varying α (left column) and varying R (right column) in their design.

(2006) and Cheung *et al.* (2012) showed significant non-linearity between the experimental pressure drop data and the theoretical predictions based on conventional rigid channel theory at large flow

rates and under high pressure drops. That is because in a bulged microchannel the measured pressure drop no longer changes linearly with flow rate (Holden *et al.*, 2003), since the microchannel's cross-section varies due to deformation, and for a constant flow rate the pressure drop changes, as explained before. However, the reported discrepancies between theoretical and experimental data seen at large flow rates are much more pronounced under high pressure drops and within channels with high aspect ratios. In these cases, the slope of the pressure drop versus flow rate curves decreases significantly as Q increases (the same trend is displayed in pressure drop versus Reynolds number curves). In fact, Cheung *et al.* (2012) reported that at low pressures (<5 kPa), the pressure drop data remained linear. All microchannels in this study have a low–moderate aspect ratio of ~2.7 and pressure drops never exceed ~2.1 kPa (maximum differential pressure that can be read with the pressure sensors used), hence it was expected that channel deformation would not have a significant effect on the results. In line with the predictions, the experimental results in Figures 3.1–3.3 seem to properly follow the linear behaviour of the theoretical profile, with a few punctual exceptions (the reason for those will be addressed further below). Thus, whilst explaining some minor deviations off the linear trend, one can conclude that the deformability of PDMS has little effect in this work.

One of the major errors in the pressure data was the inconsistency of the acquired values. The pressure sensors were statically calibrated using columns of water, however measured pressure drops did not agree with computed pressure drops for most of the times, falling systematically below the theoretically predicted curves. A closer look at Figures 3.1–3.3 shows that this systematic behaviour is more pronounced for distances AB, CD and AD, with data from stretch BC being sometimes in good agreement with the analytical model. This difference, regarding distances AB, CD and AD, is believed to be mainly caused by the built-in configuration of taps A and D, located near the inlet and outlet, respectively, of the microchannels. The roundish built-in design, with its larger than the channel's width 1.5 mm diameter (in order to accommodate the pressure sensing elements), inherently adds expansion/contraction zones to the flow's path, which alter the flow's behaviour dramatically as it passes through theses sections. Consequently, pressures A and D are measured outside of the straight channel, immediately before and after an increase (contraction) and relief (expansion) in pressure, respectively, whereas pressures B and C actually correspond to those inside the straight channel. In addition to that, tap A is placed just after the channel's inlet, where the flow is nowhere near developed. All this, naturally has an effect on the pressure drops measured across distances AB, CD and AD, and is though to be the main reason for the disparity between the results obtained from these stretches and those from stretch BC, which appear to be consistently closer to the theoretically predicted curves throughout all channels.

The configuration of pressure taps A and D is also believed to have influence on the scattering of the data observed for each Reynolds number. As explained at the start of the chapter, by plotting

$\Delta P/L$ expectation was that the measurements for each Re would all fall on the same spot of the graph, thus discarding the influence of the distance between taps. Figures 3.1–3.3 show that these are more often than not apart. This happens because the measurements from no stretch were made under the same conditions. While the measurements from stretch BC can be said to be the most 'clean', taking place where the flow is fully developed, those from the other stretches all share a common error source, yet affecting them differently. The expansion/contraction zones introduced by the configuration of taps A and D affect both the upstream and downstream single-ended pressure signals in stretch AD, whilst in stretch AB only the upstream signal is affected (tap A) and in stretch CD the same thing happens only for the downstream signal (tap D). And while these differences are true, one can go even further and conclude that none of the pressure drops measured in stretches AB, CD and AD are representative of the actual pressure difference inside the straight channel for those very same distances, precisely due to the described errors. Hence it would be impossible for the $\Delta P/L$ results from these stretches to match those from stretch BC. Therefore, the pressure drop per unit length measured across the four distances inevitably gives different results, thus explaining the inconsistency in the results for each Reynolds number.

Another effect that adds to this one, although only for distances AB and CD, is hole pressure error. This error though, is strictly associated with pressure taps B and C, since these two are connected to the main flow channel by a pair of sub-channels. Hole pressure, $P_H = P_w - P_s$, is the difference between the actual pressure at the channel's walls, P_w (i.e., the pressure that a flush-mounted sensor would measure), and the pressure measured by a recessed sensor, P_s (see Figure 3.4). This difference is derived from the normal stresses in the fluid, which cause streamlines to bend when passing over pressure holes. The tension in the streamlines causes a tensile stress to be exerted over the holes, thus making the sensors measure a lower pressure than the actual pressure in the bulk flow. Fortunately, the magnitude of this error is consistent with the size of the hole, being therefore reasonable to assume that its influence on the results from distances AB and CD can be neglected when compared to the influence of the expansion/contraction zones introduced by taps A and D. It is worth mentioning that for differential pressure measurements this effect cancels itself out, as explained by Scott (2004), hence for the measurements carried out across distance BC there is no such error.

Yet, this does not explain the gap often found between the experimental and theoretical results to its full extent. If the whole range of data collected for each microchannel is considered, one might conclude that this difference stretches out to the entire population of microchannels tested, thus being a generalised behaviour. Although if only the data obtained from stretch BC is considered, a different conclusion can be drawn. It looks as if for stretch BC, the measured pressured drop sometimes meets its theoretical prediction. Whilst for the remainder of the distances (AB, CD and AD), the results fall short of it. This happens precisely for the reasons explained above, regarding the expan-

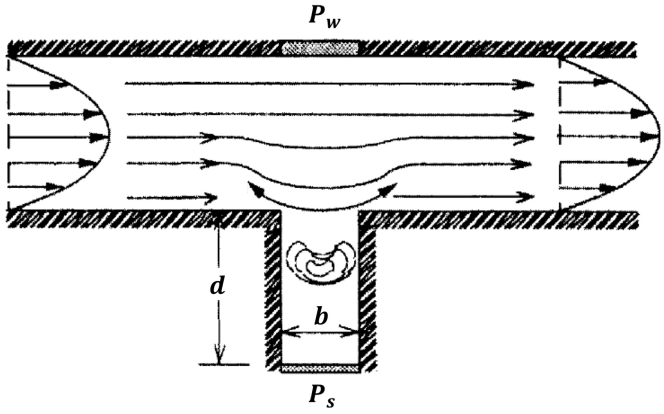

Figure 3.4: Hole pressure error - tension in the streamlines causes recessed pressure sensors, P_s, to read less than that of a flush-mounted sensor, P_w (adapted from Macosko (1994)).

sion/contraction zones introduced by the configuration of pressure taps A and D, which led to the conclusion that the only stretch that is able to provide somehow 'clean' readings is BC. Furthermore, because none of the pressure drops measured in stretches AB, BC and AD are representative of the actual pressure difference inside the channel for those distances, the analytical model naturally fails to predict them, since it is only valid for plain straight channels, not contemplating neither the contraction nor the expansion effects seen in these stretches. Thus, the mismatch between experimental and theoretical results for these stretches was, to some degree, expected from the start.

Despite BC being the best stretch to draw conclusions from, it also fails to meet the theory in a number of channels, which can only be interpreted as having been caused by either poor tap design choices (the main focus of this thesis), external effects (here characterised as effects whose control falls beyond the experimentalist's reach, hence that cannot be suppressed), or a combination of both. Having said that, it is therefore crucial to address first of all, the external effects that were likely to have caused the deviations from the theoretical profile, since these are applicable to all the measurements carried out, regardless of the distance between taps or the design of the pressure taps in which they were measured. The effects that are believed to have been the cause for this behaviour are presented herein.

Air bubbles trapped in the microchannels are though to have had the most impact in the errant pressure measurements, as these were quite frequent. The presence of air inside microchannels is known to be capable of distorting pressure readings (Campo-Deaño, 2018, Scott, 2004), either by blocking the flow or by 'absorbing' some of this pressure due to its compressibility, in a process very similar to that of the bulging of PDMS channels under pressure. Air bubbles were mostly observed inside the pressure taps and near the inlet/outlet of the channels, but never blocking the straight channel. The more or less likelihood for air bubbles to get stuck inside pressure taps B and C was

seen as a consequence of the shape of these taps, thus proving to be a relevant factor to consider in the qualitative evaluation of their measuring performance.

The anomalous results can also be attributed to a number of interfacial effects taking place near the channels inner walls. That is the case of surface tension. This phenomena translates to the flow in the form of resistance, having even blockage situations been reported in channels of small width and thickness (Kim *et al.*, 2002). Roughness of the microchannels and uncertainty in the channels dimensions are also two sources of error, yet these go back to the fabrication method. Measurements of the channels actual width, L_h (Table 2.5), clearly show that this parameter is not constant throughout the whole length of the channels. The same goes for the channels depth, L_v (Table 2.4). Moreover, part of the discrepancy may also be due to the lack of a well-controlled surface structure, since the channels were fabricated by the bonding of PDMS and glass.

Other considerations worth mentioning are those of viscosity, entrance length and 3D effects. Studies have shown that the viscosity of water retains its bulk viscosity value to within 10 % even in films as thin as 5 nm (Israelachvili, 1986). Therefore, its viscosity in the wall region is not expected to vary significantly from that of the bulk, hence discarding the influence of this parameter on the results. Regarding the entrance length, the placement of pressure taps B and C was careful not to be in a region where the flow would still be in development. Hence, no extra pressure loss due to entry effects and instabilities needs to be considered. Naturally, having a rectangular cross-section creates 3D flows inside the microchannels, yet it is believed that the level of confinement ($\Lambda = L_v/D \sim 1.3$) is not high enough to enhance these effects to such a degree that they would have impact on the results (Kenney *et al.*, 2013).

Now that the external effects which likely lead to the errant pressure measurements have been characterised, remarks on the best and worst performing pressure tap designs can be made. Although first, in order to get a sense of the true scale of the deviations observed (between the experimental and theoretical data) these must be quantified. As so, Tables 3.5–3.7 show the underlying percentage errors in the data, $\left|\Delta P_{\text{theor}} - \Delta P_{\text{exp}}\right| / \Delta P_{\text{theor}}$, for selected Reynolds numbers and per tap distance.

From all the results here displayed, the following conclusions on pressure tap design can be drawn. Naturally, the following conclusions were based on the data collected from stretch BC.

Immediately, a difference between the results from w_1 taps and those from w_2 and w_3 taps stands out. All w_1 taps show worst results than the rest, most likely due to surface tension issues, here enhanced by the sub-channels high surface area–volume ratio. This gets clear by comparing Figures 3.1, 3.2 and 3.3. Thus, one can conclude that sub-channel widths of $w \leq 54$ µm do not produce accurate results, being significantly affected by interfacial phenomena.

Regarding the remaining configurations (all w_2 and w_3 taps), another major distinction can be made, this time between the results obtained with α taps and those obtained with R taps. It seems

Table 3.5: Percentage error (%) between the experimental and theoretical data for pressure taps with w_1 = 54 µm

			Re			
		Distance	10^{-1}	10^{0}	10	10^{2}
w_1	α_1	AB	–	80.0	73.3	77.0
		BC	–	68.2	55.3	63.0
		CD	70.4	76.9	70.7	–
		AD	82.5	86.1	74.8	–
	α_2	AB	–	80.5	81.0	72.5
		BC	–	31.2	61.6	62.2
		CD	80.0	72.1	73.7	–
		AD	93.8	74.6	71.1	–
	α_3	AB	–	76.0	77.8	74.3
		BC	–	138.0	25.5	62.9
		CD	32.2	48.6	64.9	–
		AD	91.2	71.7	69.8	–
	R_1	AB	–	73.3	82.2	82.6
		BC	–	80.0	53.1	76.6
		CD	100.0	83.3	80.9	–
		AD	83.2	89.1	83.2	–
	R_2	AB	–	69.8	88.6	82.2
		BC	–	12.8	66.0	71.7
		CD	71.9	86.6	72.5	–
		AD	64.6	79.0	79.3	–
	R_3	AB	–	74.3	81.2	76.8
		BC	–	38.4	20.2	76.3
		CD	26.8	83.1	77.3	–
		AD	64.0	76.6	78.8	–

that the α taps perform worst, regardless of the w. Figures 3.2 and 3.3 are examples of just that. Also, Tables 3.6 and 3.7 lead to the same conclusion. The explanation for this difference might lie in the way the cross-section transition plays out in these taps. Whilst for the R taps this transition is smooth, for the α taps it is not. In fact, in the α_2 and α_3 taps the transition is actually quite abrupt.

Table 3.6: Percentage error (%) between the experimental and theoretical data for pressure taps with w_2 = 108 µm

			Re			
		Distance	10^{-1}	10^{0}	10	10^{2}
w_2	α_1	AB	–	52.3	51.6	–
		BC	–	91.7	31.1	39.0
		CD	89.9	62.0	59.7	–
		AD	54.8	63.0	59.8	–
	α_2	AB	–	95.1	65.6	–
		BC	–	92.5	62.9	61.9
		CD	38.1	64.0	62.5	–
		AD	74.8	43.1	58.2	–
	α_3	AB	–	43.0	58.0	63.3
		BC	–	40.5	47.0	56.2
		CD	14.9	62.3	65.3	–
		AD	49.4	15.3	65.7	–
	R_1	AB	–	52.6	58.4	52.4
		BC	–	3.3	3.3	8.5
		CD	4.5	45.1	57.0	–
		AD	46.5	60.9	55.9	–
	R_2	AB	–	32.5	54.7	–
		BC	–	13.2	1.9	16.6
		CD	31.7	45.2	45.5	–
		AD	44.0	44.2	48.2	–
	R_3	AB	–	–	–	–
		BC	–	6.5	8.0	31.2
		CD	–	–	–	–
		AD	–	–	–	–

That said, it is therefore reasonable to conclude that assuring a smooth channel–tap transition upon designing the pressure taps is key.

Taking a closer look at Tables 3.6 and 3.7, for w_2 and w_3 taps respectively, and comparing the R taps with 108 µm (w_2) and 162 µm (w_3) sub-channel width, it becomes evident that the results

Table 3.7: Percentage error (%) between the experimental and theoretical data for pressure taps with w_3 = 162 µm

			Re			
		Distance	10^{-1}	10^{0}	10	10^{2}
w_3	α_1	AB	–	69.3	86.0	74.7
		BC	–	73.3	71.5	79.8
		CD	50.5	78.1	74.6	–
		AD	59.8	81.9	77.4	–
	α_2	AB	–	64.4	79.6	67.0
		BC	–	53.9	25.2	56.8
		CD	72.4	71.4	64.1	–
		AD	70.4	63.9	68.8	–
	α_3	AB	–	63.7	79.7	65.6
		BC	–	26.7	64.8	59.6
		CD	64.2	55.0	56.2	–
		AD	18.8	66.6	56.7	–
	R_1	AB	–	71.5	57.8	53.9
		BC	–	23.9	32.6	35.6
		CD	15.2	35.6	42.1	–
		AD	24.6	15.8	32.9	–
	R_2	AB	–	58.2	64.3	–
		BC	–	38.9	16.1	30.2
		CD	26.6	45.1	43.2	–
		AD	55.1	41.4	36.6	–
	R_3	AB	–	56.2	64.6	57.0
		BC	–	35.6	15.9	40.8
		CD	41.1	35.0	52.9	–
		AD	28.7	35.9	42.8	–

obtained with the narrower sub-channel are better. So much better in fact, that with this sub-channel, of width w_2, the experimental results were found to often match those of the theoretical model. This happened particularly at the lower Reynolds numbers, $Re < 50$ (see Figure 3.2), sometimes only failing the predictions by ~2 %. The reasons for the difference observed between the results with w_2

and w_3 taps are not entirely clear, yet it is thought that it may have been caused by instabilities in the flow related to the larger sub-channel width, such as recirculation. The mild deviation from the theoretical profile at high Reynolds numbers was most likely caused by the slight compliance of the channels inner PDMS walls.

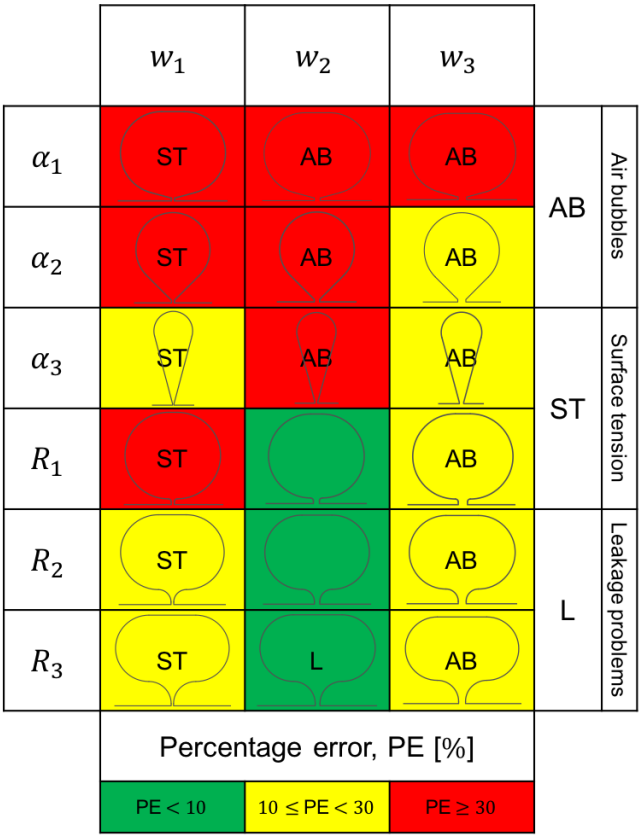

Figure 3.5: Summary of the performance of each pressure tap configuration tested.

The three w_2 tap configurations with smooth cross-section transition tested displayed a very similar behaviour, having the results from all three approximately met the theoretical predictions. From Table 3.6 it can be concluded that $R_1 = 50$ µm provides measurements with an average error below 5 %. This configuration is then, the optimal result of the parametric study. Nevertheless, all three w_2 taps are 'optimal' in the sense that they provide an environment in which pressure can be easily measured with relative accuracy and little design and fabrication constrains. This conclusion can be generalised by normalising the sub-channel's width with the width of the main channel, as so: $0.2 < w/L_h < 0.6$. Figure 3.5 summarises the results for each pressure tap design. In this Figure, three phenomena (air bubbles, surface tension and leakage problems) were highlighted as the most probable causes for the distorted pressure measurements obtained. For the pressure tap configurations that performed worst, the most likely of these effects to have caused the bad results

was pointed out. Leakage problems were seen only in one microchannel (that with sub-channel width w_2 and radius of curvature R_3) and at specific pressure taps (A and D). Fluid leaked from the pressure sensing holes through tears in the PDMS. Leakage problems have no relation with the geometry of the pressure taps, having only to do with defects that stretch back to the fabrication of the chips, mainly related to the piercing of the PDMS layers. Surface tension effects are believed to have occurred mainly in the pressure taps with the narrowest sub-channel (w_1), caused by the high surface area–volume ratio that characterises them. A colour-based qualitative analysis based on the percentage error (PE) can also be seen in Figure 3.5.

Remarks and Further Work

In chapter 3, the results from the parametric study conducted were presented. A total of 18 different pressure tap configurations were tested, using straight PDMS microfabricated channels. The incorporation of 3D printing technology in the fabrication of these channels was investigated by manufacturing molds with two stereolithography (SL) 3D printers. The different pressure tap designs were created by combining three key shape parameters: sub-channel width, w; tap cross-section transition radius of curvature, R; tap cross-section transition angle of inclination, α. Sub-channel length was kept constant for all configurations. Pressure drops were measured across different length stretches of the microchannels, in order to improve the study.

The original motivation for this work was to evaluate the influence of pressure tap design on the quality of pressure drop measurements. Measuring pressure in microfluidic devices poses serious challenges for the average experimentalist. Thus, by establishing guidelines for the optimal design of pressure taps, hopes were that some of these challenges could be resolved. In parallel, a viable solution for measuring the pressure drop caused by the presence of microbots inside vessel-like microchannels was sought. This would add new information to the study of the dynamic efficiency of these devices in real working conditions.

From the results several conclusions can be drawn. Regarding the 3D printed microchannel molds, the overall surface roughness of the standard SL ones looked smooth at first, but a closer look under the microscope revealed a much different reality. The layer interface inherent to the layer deposition process, characteristic of the fabrication technique and barely distinguishable at first, provoked a clear distortion of the microchannels. The SL-DLP molds were, in terms of detail, far superior than the conventional SL ones. Incorporating 3D printing technology in the fabrication of microfluidic molds is a definite possibility and that can be seen by the ever growing number of research publication on the topic (Bhattacharjee *et al.*, 2016). However, further development of this technology is still needed, as standard 3D printing machines struggle to produce geometries with characteristic dimensions below the 100's of micrometers with precision. Thus, 3D printing technology does not yet have the resolution required for the level of detail most microfluidic devices

demand. Instead, it can be seen as a simple, effortless and fast way of prototyping these devices, before the actual manufacturing.

Now, on the main focus of this thesis. The pressure drop per unit length versus Reynolds number data plotted, displayed a linear trend as expected. The relation $\Delta P_{BC} < \Delta P_{AB} < \Delta P_{CD} < \Delta P_{AD}$ was kept at all times. An optimal configuration for the shape of pressure taps in microchannels was achieved, within the population of tap designs tested. Out of the total 18 different pressure taps tested, 3 stood out: those with an 108 µm sub-channel width and smooth cross-section transition (that is, those in which this transition was defined by the radius of curvature R). Results obtained with these taps showed very good agreement with the theoretical model considered, having an average relative error of less than 10 %. From Table 3.6 it can be concluded that $R_1 = 50$ µm provides measurements with an average error below 5 %, hence making it an optimal choice for future pressure measurements. These conclusions can be generalised by normalising the sub-channel's width with the width of the main channel: $0.2 < w/L_h < 0.6$. Generally, some non-linearity was detected in the results, yet only for the higher Reynolds numbers ($Re \geq 50$). This was caused by the compliance of the channels inner PDMS walls with increasing pressure. Since the measured pressure drops inside the microchannels were rather low, never exceeding ~2.1 kPa, the magnitude of this error was not worrying at lower Reynolds numbers. The measurements from channel stretches AB, CD and AD were influenced by the built-in configuration of pressure taps A and D, falling systematically far from the theoretically predicted curve. The configuration of these taps inherently adds expansion/contraction zones to the channels, which naturally disturb the flow. Hence, the theoretical curve used as reference ceases to apply to the affected stretches, since it was computed for constant cross-section straight channels. Stretch BC was then, the most significant. For this stretch no entry effects had to be accounted for, given its location far from the microchannel inlet. Anomalous behaviour in the results from this stretch was linked to air bubbles stuck inside the pressure taps, surface tension effects and geometrical imperfections related to the fabrication method. The more or less likelihood for these effects to develop can be related to the shape of the taps. With that in mind, the following conclusions were drawn:

- Pressure taps with a small sub-channel width ($w \leq 54$ µm) are likely to be affected by surface tension phenomena;
- Pressure tap shapes containing edges or other similar geometrical features (α taps) perform worst than those with a smooth contour (R taps);
- Pressure taps with a sub-channel width of 108 µm produce better results than those with an 162 µm sub-channel width, in which instabilities, such as recirculating flow, might occur.

Naturally, the follow up to this study would be to measure the pressure drop induced by the pres-

ence of the microbot models designed at the start, using the three pressure tap configurations that showed the best results. Inevitably, the substitution of DI water with a blood analogue fluid would happen, in order to replicate the actual flow conditions inside the human circulatory system. Ideally, real whole blood should be used but its manipulation and *in vitro* flow dynamics study present a number of complications regarding cost, safety and ethics issues (Campo-Deaño *et al.*, 2013). This shift in working fluid, would mean an entirely different approach to the flow dynamics inside the microchannels, since blood is a non-Newtonian fluid. Rheology would have to be addressed, as well as flow instabilities that naturally arise given the viscoelastic nature of the fluid, and a whole new range of dimensionless numbers would need to be introduced, such as the Weissenberg number, W_i. In the presence of an obstacle (e.g., a microbot prototype), the pressure drops obtained with a non-Newtonian fluid would be significantly higher to those achieved using a Newtonian fluid. Moreover, the transient response of the pressure drop upon changing the flow rate would also increase, taking longer to achieve a steady-state condition.

Another addition that could be made in the future is that of replicating the blood flow's pulsatile regime, characteristic of the heart pumping actions. This could be made by loading a custom flow profile into the syringe pump. Also, μPIV and streakline photography techniques could be used to further characterise the flow dynamics in the microchannels.

Publications

- Publications in refereed conferences

  -Pinto, T.P. and Campo-Deaño, L. (April, 2018). Parametric study for the optimal design of pressure taps in microchannels. Abstract of poster presentation submitted to the 12th Annual European Rheology Conference (AERC 2018). Sorrento, Italy.

  -Pinto, T.P. and Campo-Deaño, L. (September, 2018). Pressure Drop Measurements in Microchannels: Influence of the Tap Design. Proceedings of the EUROMECH Colloquium 603 - Dynamics of micro and nano systems. Porto, Portugal.

- Participation in conferences

  -Pinto, T.P. and Campo-Deaño, L. (April, 2018). Parametric study for the optimal design of pressure taps in microchannels. Poster presented at the 12th Annual European Rheology Conference (AERC 2018). Sorrento, Italy.

  -Pinto, T.P. and Campo-Deaño, L. (September, 2018). Pressure Drop Measurements in Microchannels: Influence of the Tap Design. Oral presentation at the EUROMECH Colloquium 603 - Dynamics of micro and nano systems. Porto, Portugal.

Bibliography

Adzima, B.J. and Velankar, S.S. 2006. Pressure drops for droplet flows in microfluidic channels. *Journal of Micromechanics and Microengineering*, **16**, 1504–1510.

Ahn, C.H.; Choi, J.; Beaucage, G.; Nevin, J.H.; Lee, J.; Puntambekar, A. and Lee, J.Y. 2004. Disposable smart lab on a chip for point-of-care clinical diagnostics. *Proceedings of the IEEE*, **92**, 154–173.

Ateya, D.A.; Shah, A.A. and Hua, S.Z. 2005. Impedance-based response of an electrolytic gas bubble to pressure in microfluidic channels. *Sensors and Actuators A: Physical*, **122**, 235–241.

Banerjee, N.; Xie, Y.; Pandey, S.S. and Mastrangelo, C.H. 2014. Pressure sensing in microfluidic environments with low-leakage microballoons. *Pages 114–116 of: 18th International Conference on Miniaturized Systems for Chemistry and Life Sciences, MicroTAS 2014.*

Berger, S.A.; Goldsmith, W. and Lewis, E.R. 1996. *Introduction to Bioengineering.* Oxford University Press.

Bhattacharjee, N.; Urrios, A.; Kang, S. and Folch, A. 2016. The upcoming 3D-printing revolution in microfluidics. *Lab Chip*, **16**, 1720–1742.

Bruus, H. 2008. *Theoretical Microfluidics.* Oxford University Press.

Campo-Deaño, L. 2018. *Fluid-Flow Characterization in Microfluidics.* Springer International Publishing. Pages 53–71.

Campo-Deaño, L.; Galindo-Rosales, F.J.; Pinho, F.T.; Alves, M.A. and Oliveira, M.S.N. 2011. Flow of low viscosity Boger fluids through a microfluidic hyperbolic contraction. *Journal of Non-Newtonian Fluid Mechanics*, **166**, 1286–1296.

Campo-Deaño, L.; Dullens, R.P.A.; Aarts, D.G.A.L.; Pinho, F.T. and Oliveira, M.S.N. 2013. Viscoelasticity of blood and viscoelastic blood analogues for use in polydymethylsiloxane in vitro models of the circulatory system. *Biomicrofluidics*, **7**, 034102.

Carrozza, M.C.; Dario, P. and Jay, L.P.S. 2003. Micromechatronics in surgery. *Transactions of the Institute of Measurement and Control*, **25**, 309–327.

Catarino, S.; Lima, R. and Minas, G. 2017. 12 - Smart devices: Lab-on-a-chip. *Pages 331–369 of: Bioinspired Materials for Medical Applications*. Woodhead Publishing.

Chang, W.Y.; Chu, C.H. and Lin, Y.C. 2008. A Flexible Piezoelectric Sensor for Microfluidic Applications Using Polyvinylidene Fluoride. *IEEE Sensors Journal*, **8**, 495–500.

Chen, Y.; Chan, H.N.; Michael, S.A.; Shen, Y.; Chen, Y.; Tian, Q.; Huang, L. and Wu, H. 2017. A microfluidic circulatory system integrated with capillary-assisted pressure sensors. *Lab Chip*, **17**, 653–662.

Cheung, P.; Toda-Peters, K. and Shen, A.Q. 2012. In situ pressure measurement within deformable rectangular polydimethylsiloxane microfluidic devices. *Biomicrofluidics*, **6**, 026501.

Chung, K.; Lee, H. and Lu, H. 2009. Multiplex pressure measurement in microsystems using volume displacement of particle suspensions. *Lab Chip*, **9**, 3345–3353.

Coleman, H. and Steele, W.G. 2009. *Experimentation, Validation, and Uncertainty Analysis for Engineers, Fourth Edition*. John Wiley & Sons, Inc.

Duffy, D.C.; McDonald, J.C.; Schueller, O.J.A. and Whitesides, G.M. 1998. Rapid Prototyping of Microfluidic Systems in Poly(dimethylsiloxane). *Analytical Chemistry*, **70**, 4974–4984.

Eaton, W.P. and Smith, J.H. 1997. Micromachined pressure sensors: review and recent developments. *Smart Materials and Structures*, **6**, 530–539.

Effenhauser, C.; Bruin, G.; Aran, P. and Ehrat, M. 1997. Integrated Capillary Electrophoresis on Flexible Silicone Microdevices: Analysis of DNA Restriction Fragments and Detection of Single DNA Molecules on Microchips. *Analytical Chemistry*, **69**, 3451–3457.

Ergeneman, O.; Chatzipirpiridis, G.; Pokki, J.; Marin-Suárez, M.; Sotiriou, G.A.; Medina-Rodriguez, S.; Sanchez, J.F.F.; Fernandez-Gutiérrez, A.; Pane, S. and Nelson, B.J. 2012. In Vitro Oxygen Sensing Using Intraocular Microrobots. *IEEE Transactions on Biomedical Engineering*, **59**, 3104–3109.

Feynman, R.P. 1992. There's Plenty of Room at the Bottom. *Journal of Microelectromechanical Systems*, **1**, 60–66.

Gervais, T.; El-Ali, J.; Ǵunther, A. and Jensen, K.F. 2006. Flow-induced deformation of shallow microfluidic channels. *Lab Chip*, **6**, 500–507.

Gravesen, P.; Branebjerg, J. and Jensen, O.S. 1993. Microfluidics - A Review. *Journal of Micromechanics and Microengineering*, **3**, 168.

Grundmann, A.; Clavica, F.; Landolt, A.; Barrett, M.; Weber, B. and Obrist, D. 2015. *Measurement of Fluid Pressure in Microchannels*.

Gupta, K.; Kim, D.; Ellison, D.; Smith, C.; Kundu, A.; Tuan, J.; Suh, K. and Levchenko, A. 2010. Lab-on-a-chip devices as an emerging platform for stem cell biology. *Lab Chip*, **10**, 2019–2031.

Hardy, B.S.; Uechi, K.; Zhen, J. and Kavehpour, H.P. 2009. The deformation of flexible PDMS microchannels under a pressure driven flow. *Lab Chip*, **9**, 935–938.

Hetsroni, G.; Mosyak, A.; Pogrebnyak, E. and Yarin, L.P. 2005. Fluid flow in micro-channels. *International Journal of Heat and Mass Transfer*, **48**, 1982–1998.

Holden, M.A.; Kumar, S.; Beskok, A. and Cremer, P.S. 2003. Microfluidic diffusion diluter: Bulging of PDMS microchannels under pressure-driven flow. *Journal of Micromechanics and Microengineering*, **13**, 412–418.

Hosokawa, K.; Hanada, K. and Maeda, R. 2002. A polydimethylsiloxane (PDMS) deformable diffraction grating for monitoring of local pressure in microfluidic devices. *Journal of Micromechanics and Microengineering*, **12**, 1.

Huang, P.Y. and Feng, J. 1995. Wall effects on the flow of viscoelastic fluids around a circular cylinder. *Journal of Non-Newtonian Fluid Mechanics*, **60**, 179–198.

Hwang, Y.; Paydar, O.H. and Candler, R.N. 2015. 3D printed molds for non-planar PDMS microfluidic channels. *Sensors and Actuators A: Physical*, **226**, 137–142.

Israelachvili, J.N. 1986. Measurement of the viscosity of liquids in very thin films. *Journal of Colloid and Interface Science*, **110**, 263–271.

Kartalov, E.P.; Maltezos, G.; Anderson, W.F.; Taylor, C.R. and Scherer, A. 2007. Electrical microfluidic pressure gauge for elastomer microelectromechanical systems. *Journal of Applied Physics*, **102**, 084909.

Kenney, S.; Poper, K.; Chapagain, G. and Christopher, G.F. 2013. Large Deborah number flows around confined microfluidic cylinders. *Rheologica Acta*, **52**, 485–497.

Kestenbaum, H.; Oliveira, A.L.; Schmidt, W.; Schüth, F.; Ehrfeld, W.; Gebauer, K.; Löwe, H.; Richter, T.; Lebiedz, D.; Untiedt, I. and Züchner, H. 2002. Silver-Catalyzed Oxidation of Ethylene to Ethylene Oxide in a Microreaction System. *Industrial & Engineering Chemistry Research*, **41**, 710–719.

Kim, D.S.; Lee, K.; Kwon, T.H. and Lee, S.S. 2002. Micro-channel filling flow considering surface tension effect. *Journal of Micromechanics and Microengineering*, **12**, 236–246.

Kirby, B.J. 2010. *Micro- and Nanoscale Fluid Mechanics: Transport in Microfluidic Devices.* Cambridge University Press.

Kohl, M.J.; Abdel-Khalik, S.I.; Jeter, S.M. and Sadowski, D.L. 2005a. An experimental investigation of microchannel flow with internal pressure measurements. *International Journal of Heat and Mass Transfer*, **48**, 1518–1533.

Kohl, M.J.; Abdel-Khalik, S.I.; Jeter, S.M. and Sadowski, D.L. 2005b. A microfluidic experimental platform with internal pressure measurements. *Sensors and Actuators A: Physical*, **118**, 212–221.

Krishnan, S. and Kaman, A. 2010. Effect of Blockage Ratio on Drag and Heat Transfer from a Centrally Located Sphere in Pipe Flow. *Engineering Applications of Computational Fluid Mechanics*, **4**, 396–414.

Kuoni, A.; Holzherr, R.; Boillat, M. and Rooij, N.F. 2003. Polyimide membrane with ZnO piezoelectric thin film pressure transducers as a differential pressure liquid flow sensor. *Journal of Micromechanics and Microengineering*, **13**, S103–S107.

Lauga, E.; Brenner, M. and Stone, H. 2007. *Microfluidics: The No-Slip Boundary Condition.* Springer Berlin Heidelberg. Pages 1219–1240.

Lee, D. and Choi, Y. 2008. A novel pressure sensor with a PDMS diaphragm. *Microelectronic Engineering*, **85**, 1054–1058.

Lei, K.F.; Lee, K. and Lee, M. 2012. Development of a flexible PDMS capacitive pressure sensor for plantar pressure measurement. *Microelectronic Engineering*, **99**, 1–5.

Li, H.; Luo, C.X.; Ji, H.; Ouyang, Q. and Chen, Y. 2010. Micro-pressure sensor made of conductive PDMS for microfluidic applications. *Microelectronic Engineering*, **87**, 1266–1269.

Luttge, R. 2011. Chapter 7 - Microfluidic Components, Devices and Integrated Lab-on-a-Chip Systems. *Pages 199–233 of: Microfabrication for Industrial Applications.* William Andrew Publishing.

Mack, M.J. 2001. Minimally invasive and robotic surgery. *JAMA*, **285**, 568–572.

Macosko, C.W. 1994. *Rheology: Principles, Measurements, and Applications.* John Wiley & Sons, Inc.

Marrian, C.R.K. and Tennant, D.M. 2003. Nanofabrication. *Journal of Vacuum Science & Technology A*, **21**, S207–S215.

Martel, S. 2012. *Magnetic Microbots to Fight Cancer.* https://spectrum.ieee.org/robotics/medical-robots/magnetic-microbots-to-fight-cancer.

Martínez-Aranda, S.; Galindo-Rosales, F.J. and Campo-Deaño, L. 2016. Complex flow dynamics around 3D microbot prototypes. *Soft Matter*, **12**, 2334–2347.

McDonald, J.C.; Duffy, D.C.; Anderson, J.R.; Chiu, D.T.; Wu, H.; Schueller, O.J.A. and Whitesides, G.M. 2000. Fabrication of microfluidic systems in poly(dimethylsiloxane). *ELECTROPHORESIS*, **21**, 27–40.

McKinley, G.H.; Rodd, L.E.; Oliveira, M.S.N. and Cooper-White, J. 2007. Extensional flows of polymer solutions in microfluidic converging/diverging geometries. *Journal of Central South University of Technology*, **14**, 6–9.

Munson, B.R.; Okiishi, T.H.; Huebsch, W.W. and Rothmayer, A.P. 2013. *Fluid Mechanics, Seventh Edition.* John Wiley & Sons, Inc.

Nelson, B.J.; Kaliakatsos, I.K. and Abbott, J.J. 2010. Microrobots for Minimally Invasive Medicine. *Annual Review of Biomedical Engineering*, **12**, 55–85.

Ng, J.M.K.; Gitlin, I.; Stroock, A.D. and Whitesides, G.M. 2002. Components for integrated poly(dimethylsiloxane) microfluidic systems. *ELECTROPHORESIS*, **23**, 3461–3473.

Nguyen, N. and Wereley, S.T. 2006. *Fundamentals and Applications of Microfluidics.* Artech House.

Oosterbroek, R.E.; Lammerink, T.S.J.; Berenschot, J.W.; Krijnen, G.J.M.; Elwenspoek, M.C. and van denBerg, A. 1999. A micromachined pressure/flow-sensor. *Sensors and Actuators A: Physical*, **77**, 167–177.

Papautsky, I.; Brazzle, J.; Ameel, T. and Frazier, A.B. 1999. Laminar fluid behavior in microchannels using micropolar fluid theory. *Sensors and Actuators A: Physical*, **73**, 101–108.

Park, C.S.; Kang, B.S.; Lee, D.W.; Choi, T.Y. and Choi, Y.S. 2007. Fabrication and characterization of a pressure sensor using a pitch-based carbon fiber. *Microelectronic Engineering*, **84**, 1316–1319.

Pipe, C.J. and McKinley, G.H. 2009. Microfluidic rheometry. *Mechanics Research Communications*, **36**, 110–120.

Quake, S.R. and Scherer, A. 2000. From Micro- to Nanofabrication with Soft Materials. *Science*, **290**(5496), 1536–1540.

Rodd, L.E.; Cooper-White, J.J.; Boger, D.V. and McKinley, G.H. 2007. Role of the elasticity number in the entry flow of dilute polymer solutions in micro-fabricated contraction geometries. *Journal of Non-Newtonian Fluid Mechanics*, **143**, 170–191.

Scott, T.P. 2004. *Contraction/expansion Flow of Dilute Elastic Solutions in Microchannels.* M.S. Thesis, Mechanical Engineering Department, MIT.

Shoji, S. and Esashi, M. 1994. Microflow devices and systems. *Journal of Micromechanics and Microengineering*, **4**, 157.

Tabeling, P. 2005. *Introduction to Microfluidics.* Oxford University Press.

Tng, D. Jian, H.; Song, P.; Hu, R.; Yang, C.; Tan, C.H. and Yong, K. 2015. Standalone Lab-on-a-Chip Systems toward the Evaluation of Therapeutic Biomaterials in Individualized Disease Treatment. *ACS Biomaterials Science & Engineering*, **1**, 1055–1066.

Unger, M.A.; Chou, H.; Thorsen, T.; Scherer, A. and Quake, S.R. 2000. Monolithic Microfabricated Valves and Pumps by Multilayer Soft Lithography. *Science*, **288**, 113–116.

Voronov, R.S.; Papavassiliou, D.V. and Lee, L.L. 2008. Review of Fluid Slip over Superhydrophobic Surfaces and Its Dependence on the Contact Angle. *Industrial & Engineering Chemistry Research*, **47**, 2455–2477.

Waheed, S.; Cabot, J.M.; Macdonald, N.P.; Lewis, T.; Guijt, R.M.; Paull, B. and Breadmore, M.C. 2016. 3D printed microfluidic devices: enablers and barriers. *Lab Chip*, **16**, 1993–2013.

White, F.M. 2006. *Viscous Fluid Flow, Third Edition.* McGraw-Hill.

Whitesides, G.M. 2006. The origins and the future of microfluidics. *Nature*, **442**, 368–373.

Wu, C.; Liao, W. and Tung, Y. 2011. Integrated ionic liquid-based electrofluidic circuits for pressure sensing within polydimethylsiloxane microfluidic systems. *Lab Chip*, **11**, 1740–1746.

Xia, Y. and Whitesides, G.M. 1998. Soft Lithography. *Annual Review of Materials Science*, **28**, 153–184.

Yesilata, B.; Öztekin, A.; Neti, S. and Kazakia, J. 2000. Pressure Measurements in Highly Viscous and Elastic Fluids. *Journal of Fluids Engineering*, 626–633.

Yi, H.; Lee, H. and Cho, D. 2017. 3D Printing of Organs-On-Chips. *Bioengineering*, **4**.

Zhu, W.; Li, J.; Leong, Y.J.; Rozen, I.; Qu, X.; Dong, R.; Wu, Z.; Gao, W.; Chung, P.H.; Wang, J. and Chen, S. 2015. 3D-Printed Artificial Microfish. *Advanced Materials*, **27**, 4411–4417.

Appendices

Annual European Rheology Conference
April 17-20, 2018 - Sorrento, Italy

Parametric study for the optimal design of pressure taps in microchannels

Tomás Rodrigues PINTO and Laura CAMPO-DEAÑO

Centro de Estudos de Fenómenos de Transporte (CEFT), Departamento de Engenharia Mecânica, Faculdade de Engenharia da Universidade do Porto, R. Dr. Roberto Frias, 4200-465 Porto, Portugal.

The recent advances in microfabrication techniques allowed the use of microfluidics for characterizing the complex flow dynamics around different microbot prototypes to be used in biomedicine [1]. However, the complete fluid flow characterization must include the determination of the pressure drop induced by the presence of the prototype in order to analyze the dynamic efficiency of these devices, which is a challenging task. Therefore, the final aim of this work is to assess the dynamic efficiency of microbots in complex fluid flows analogue to human blood flows. For that end, the assessment of the pressure drop originated by the presence of the prototypes is essential. The specific objective of this research is the study of the influence of different shape parameters in the design of the pressure taps in microchannels. Polydimethylsiloxane (PDMS) microchannels were fabricated with different 2D microbot prototypes. Different variables were considered in the design of the taps and the secondary microchannels connecting the taps: width of the secondary channel (w), radius of curvature of the tap (R), angle between the tap and the secondary channel (α) and length of the secondary channel (L). Pressure drop measurements were carried out with different combinations of theses variables in order to determine the optimal design.

[1] Martínez-Aranda, S., Galindo-Rosales, F. J. and Campo-Deaño, L. (2016). Complex flow dynamics around 3D microbot prototypes. *Soft Matter*, 12, 2334-2347.

Annual European Rheology Conference
co-organized with XV Meeting of the Italian Society of Rheology-SIR

Parametric study for the optimal design of pressure taps in microchannels

T. R. Pinto and L. Campo-Deaño

CEFT, Faculdade de Engenharia da Universidade do Porto, Rua Dr. Roberto Frias, 4200-465 Porto, Portugal

Motivation and objectives

The recent advances in microfabrication techniques allowed the use of microfluidics for characterizing the complex flow dynamics around different microbot prototypes to be used in biomedicine [1]. However, the complete fluid flow characterization must include the determination of the pressure drop induced by the presence of the prototype in order to analyze the dynamic efficiency of these devices, which is a challenging task. Therefore, the final aim of this work is to assess the dynamic efficiency of microbots in complex fluid flows analogue to human blood flows. For that end, the assessment of the pressure drop originated by the presence of the prototypes is essential. The specific objective of this research is the study of the influence of different shape parameters in the design of pressure taps in microchannels. For that purpose, polydimethylsiloxane (PDMS) microchannels were fabricated with different 2D microbot prototypes inside.

Main problems in the determination of pressure drop in microchannels

Several problems associated with tap design have been reported, such as air bubbles trapped in the sub-channels leading to the taps which are very common and have a negative impact on the accuracy of the readings. Surface tension issues have also been reported, as they distort the reading in excess, by adding a residual pressure, associated with the surface tension phenomena. Problems like these are closely related to poorly designed, long and narrow sub-channels, that promote such undesired effects.

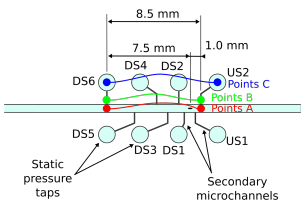

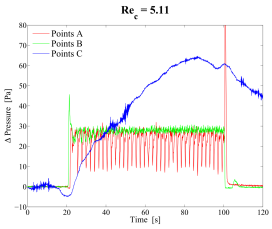

Martínez-Aranda, S. (2014).

Proposed solution

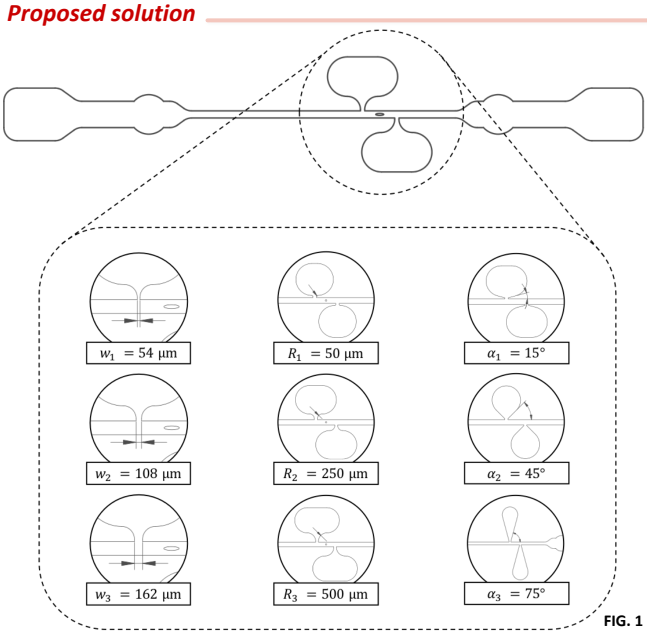

FIG. 1 CAD designs.

Aiming for the determination of the optimal tap design, a parametric study was conceived. In that sense, three variables were considered in the design of these taps and the secondary sub-channels connecting them to the main flow channel: width of the sub-channel (w), radius of curvature between the sub-channel and the tap (R) and angle between the sub-channel and the tap (α). Up to 18 different combinations can be arranged with these shape parameters. Which leads to a total of 54 microchannels, considering the two microbot shapes tested (circular and elliptical), as well as reference channels.

	w (µm)	R (µm)	α (°)
1	54	50	15
2	108	250	45
3	162	500	75

TAB. 1 Shape parameters.

Pressure drop measurements

Pressure sensors from Silicon Microstructures, Inc. were used, each with its own operating pressure range: SM5852-015W (0-0.05 PSI), SM5852-001 (0-0.15 PSI) and SM5852-003 (0-0.3 PSI). Previous calibration of the sensors was conducted, as depicted below.

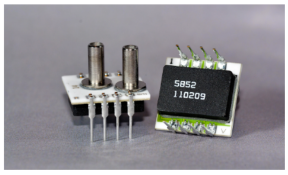

FIG. 3 Differential pressure sensors used in this study.

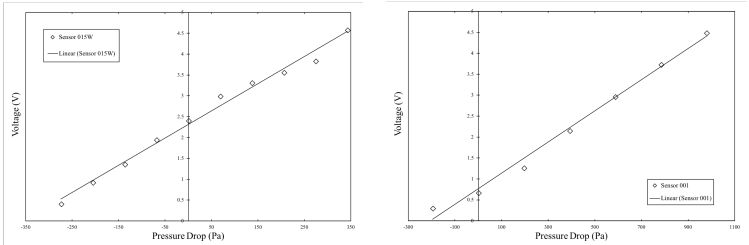

FIG. 4 Example of calibration curves for sensors 015W and 001.

Device fabrication

Three different master molds were used for the soft lithography manufacturing of the PDMS microchannels: a silicon substract SU-8 coated mold and two 3D printed molds, one by stereolithography (SLA) and the other by digital light processing (DLP).

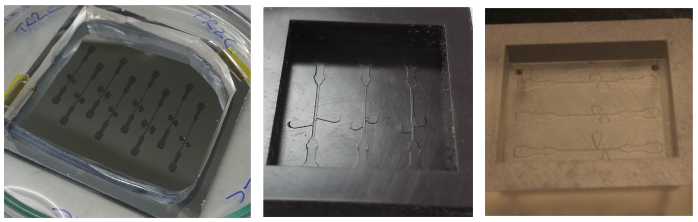

FIG. 2 From left to right: SU-8, SLA and DLP master molds with microchannel negative engravings.

Analytical results

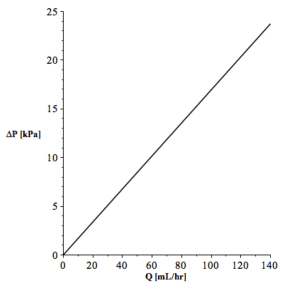

The experimental data gathered from reference microbot-free microchannels will be compared to the analytical solution for pressure drop in rectangular microchannels and laminar Newtonian flow [2]

$$\Delta P = \frac{12LQ(1+\frac{H}{w})\mu}{wH^3}$$

FIG. 5 Pressure drop-flow rate analytical solution for rectangular microchannels.

Remarks

Understanding the influence of tap design on the quality of pressure measurements is of key importance for the development of not only microbot technology but also the microfluidics field as a whole. An optimal configuration for the shape of pressure taps in microchannels is being studied and guidelines on how to correctly design them are in development.

Acknowledgements

Authors acknowledge Dr. Francisco J. Galindo-Rosales for invaluable guidance in the experimental techniques.

References

[1] Martínez-Aranda, S., Galindo-Rosales, F. J. and Campo-Deaño, L. (2016). Soft Matter, 12, 2334-2347.

[2] Pipe, C. J. and McKinley, G.H. (2009). Mechanics Research Communications, 36, 110-120.

COMPETE
GOVERNO DE PORTUGAL
UNIÃO EUROPEIA
POPH
FCT
Fundação para a Ciência e a Tecnologia

EUROMECH Colloquium 603
Dynamics of micro and nano systems
5 – 7 September 2018, Porto, Portugal

Pressure Drop Measurements in Microchannels: Influence of the Tap Design

Tomás R. Pinto and Laura Campo-Deaño

Centro de Estudos de Fenómenos de Transporte (CEFT), Departamento de Engenharia Mecânica,
Faculdade de Engenharia da Universidade do Porto, Rua Dr. Roberto Frias, 4200-465, Porto, Portugal
up201303703@fe.up.pt
campo@fe.up.pt

Summary. Microfluidics techniques have been recently used for the characterization of the complex flow dynamics around microbot prototypes to be used in biomedicine. For a complete fluid flow characterization, the determination of the pressure drop induced by the presence of these prototypes as they swim through the circulatory system is of key importance. The design of suitable microchannels able to mimic the main features of the circulatory system, including also pressure taps, constitutes a challenging task, due to the inherent difficulties in finding a proper configuration. The specific objective of this research is to study the influence of various shape parameters in the design of pressure taps, so that an optimal configuration is achieved.

Keywords: Microbots, microchannels, pressure taps, complex fluid flows.

1 Introduction

Microbots have come to be developed for, among other purposes, industrial applications and biomedicine [1, 2]. In the biomedicine field, once the technology matures, microbots will allow for precise and delicate minimally invasive procedures throughout the human body. As a matter of fact, the use of these microdevices as surgical tools will most certainly revolutionize areas such as cancer-fighting [3], drug delivery [4] and intraocular oxygen-sensing [5]. Moreover, several patient-oriented benefits are to be expected given the minimally invasive character of this surgical system. Some of the expected benefits are related to the reduction of recovery time, risk of infection and medical complications [6, 7].

In order to push the development of this concept forward, the dynamic efficiency and flow performance of microbots inside the human body are key topics that need to be fully understood. Therefore, the determination of the pressure drop originated by their presence in blood-vessels and other similar capillaries is a notoriously important matter that will undoubtedly add to this ongoing worldwide project that is microbots, contributing to its materialization in years to come.

Measuring pressure drops at microscale is not an easy task though, and several problems have been reported, mainly associated with tap design issues. Problems such as air bubbles trapped in the sub-channels leading to the taps are very common and have a negative impact on the accuracy of the readings, affecting the sensitivity of the overall measuring process and distorting the measurement itself. Surface tension issues have also been reported. They distort the reading in excess, by adding a residual pressure, associated with the surface tension phenomena, to the intended pressure drop that is being measured. Problems like these are closely related to poorly designed, long and narrow sub-channels, that promote such undesired effects.

This study aims to eradicate such difficulties when measuring pressure drops in microchannels, by developing guidelines on correct pressure tap design and proposing an optimal tap configuration for precise and problem-free readings.

2 Pressure measurement within microfluidic devices

Besides commercially available external pressure transducers, the most straightforward means of obtaining pressure data with little to no design modifications, several other methods for determining pressure drops in microchannels have been reported, differing from each other in measuring technique.

For instance, the base material from which the microchannels are made, thanks to its inherent properties, might allow for specific pressure measuring methods. This is the case of silicon based microchan-

nels, a rather decaying solution for microdevice fabrication thanks to the much practical and cheaper PDMS alternative. Several research groups [8, 9] have been using silicon based microchannels, since these can be routinely etched, allowing for several sensing elements to be incorporated. But as mentioned before, even though silicon is a good alternative from which to fabricate precise microfluidic devices, it has its drawbacks. It comes at a high cost, the whole fabrication process is time consuming and has some intricate steps along the way, and the fact that it is an opaque material, not allowing for the straightforward visualization of the devices, doesn't come in handy either.

As an alternative, microchannels made of polydimethylsiloxane (PDMS) are commonly used. They come at a lower cost and their fabrication process is less time consuming, while keeping the same step structure and technology requirements. Moreover, PDMS is optically transparent, which is good for quick first look impressions. When it comes to pressure sensing with PDMS, several research groups [10, 11] have used its elastic nature to their advantage, relating the deflection of the walls to the channel's pressure by means of imaging tools such as microscopes. However, this method and others alike often require additional fabrication steps in order to incorporate extra channel layers onto the main PDMS flow channels, fluorescent particles, or even to introduce separate probing fluids.

In the present study, the most practical solution for pressure drop measuring will be used, external pressure transducers. This is the best way to measure pressure drops in PDMS microchannels without the hassle of having to do major design modifications [12]. In addition to only requiring an external sensor and no design or extra microfluidic device incorporation requirements, pressure transducers can easily be coupled with a data acquisition card, allowing for real-time dynamic measurements.

3 Device design and fabrication

In this study, microchannels were fabricated in close resemblance to the blood-vessels that comprise the vast capillary network that is the human circulatory system. In this system one can find a wide range of flow conditions, deeply related to the proximity of the heart. The further away from the heart, the more variations the blood flow will present. The flow can range from larger vessels with a 2-3 mm characteristic diameter, where Re ~ 3000 having a strong pulsating component, to the smallest capillaries with a 20-30 μm characteristic diameter, where Re ≤ 1 and the flow is almost constant [13]. Taking into consideration that the smaller the vessel, the greater the non-Newtonian properties of the blood flow are, this work focuses on the medium to small scale (diameter < 1 mm) conduits of the human body.

Straight rectangular microchannels, with 270 μm across and 100 μm in depth, were designed, each one with a 2D microbot prototype in the center of the channel. The microchannels are all 10 mm long and the prototypes are located ~ 2.9 mm away from the inlet, in order to avoid any entry effects and ensure that enough space is left for the flow to fully develop again, downstream from the microbot, hence avoiding exit effects also. Two different prototypes were considered: a circular one and an elliptical one, with an aspect ratio of 1:4. Also, reference microchannels with no prototype inside were conceived for validation purposes.

In order to assess the pressure drop originated by the presence of the microbots, a couple of pressure taps, placed up and downstream and equally distant from their centroid, leading from the main flow channel were added. These taps provide the fluidic connection to the external pressure transducer, via the transducer ports inserted in them. The fluid flows through the main channel, via inlet and outlet ports.

Table 1. Shape parameters and respectively assigned values

	w (μm)	R (μm)	α ($^\circ$)
1	54	50	15
2	108	250	45
3	162	500	75

Aiming for the determination of the optimal tap design, a parametric study was conducted. In that sense, three variables were considered in the design of these taps and the secondary sub-channels con-

necting them to the main flow channel (Table 1): width of the sub-channel (w), radius of curvature between the sub-channel and the tap (R) and angle between the sub-channel and the tap (α).

Up to 18 different combinations can be arranged with these shape parameters. Which leads to a total of 54 microchannels, considering the two microbot shapes tested (squared and elliptical), as well as the reference channels. Figure 1 shows a microchannel with some of the pressure tap configurations possible.

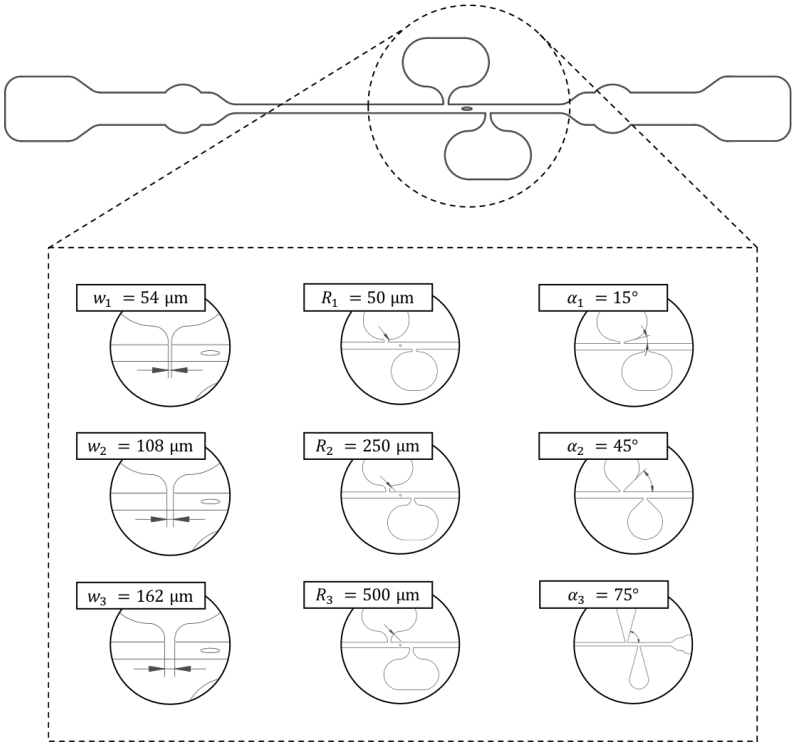

Figure 1. CAD designs for different pressure tap configurations.

PDMS microchannels were made using soft lithography techniques [14], and afterwards, bonded to glass microscope slides, that had been previously PDMS spin coated. Two different methods were used for the fabrication of the microchannel molds: on one hand, silicon substrate SU-8 coated master molds using photolithography; and, on the other hand, 3D printed molds were fabricated, in order to assess the degree of resolution of this technology and whether it can be used as an alternative for SU-8 molds. Two distinct 3D printing methods were used, both laser-based: stereolithography (SLA) and digital light processing (DLP).

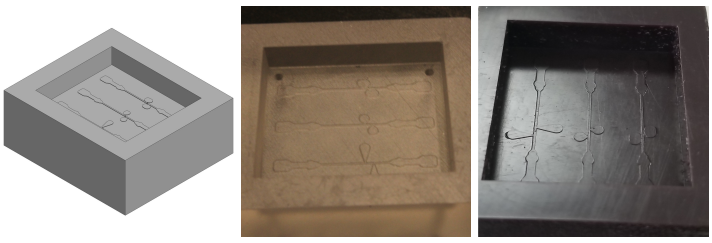

Figure 2. From left to right, the 3D CAD model and resulting 3D printed SLA and DLP molds.

The stereolithography printer's (Formlabs® Form 2) X:Y resolution is set at 150 μm (it has a laser spot size of 140 μm), while the digital light processing one (Creative CADworks® MiiCraft μMicrofluidics Edition) is capable of producing pieces with an X:Y resolution of up to 30 μm, making it more adequate for intricately detailed pieces (Figure 2).

4 Pressure drop measurements

Two blood analogues were used as working fluids, a Newtonian one and a non-Newtonian one. They are considered blood analogues in the sense that they are able to reproduce the viscosity curve and the elastic character of the whole human blood as a bulk [1, 15], making them adequate for this work.

Before carrying out any pressure measurements, the external transducers were calibrated. The calibration curves obtained were later used to relate the transducers's measured voltage output at a specific flow rate to a differential pressure drop measurement.

Once the transducers were calibrated, the tests were conducted and the pressure readings plotted in relation to flow rate. The experimental data gathered from the reference plain microchannels, which have no microbot prototype inside, was compared to pressure drop-flow rate curves obtained analytically for rigid walls rectangular cross section microchannels.

5 Final remarks

An optimal configuration for the shape of pressure taps in microchannels was achieved and several guidelines on how to correctly design them were developed. More experimental work is still needed for a complete characterization of the pressure drop obtained with the different configurations. Nevertheless, it is possible to conclude that 3D printing technology does not yet have the resolution required for the level of detail most microfluidic devices demand. Instead, it can be seen as a simple and fast way of materializing and prototyping microdevices before a final manufacturing. The overall surface roughness of the SLA molds looked smooth, but a closer look under the microscope revealed a much different reality. The layer interface inherent to the layer deposition process, characteristic of the fabrication technique and barely distinguishable at first, provoked a clear distortion of the microchannels. Regarding the DLP molds, the level of detail achieved was clearly higher when placed side by side with the SLA ones.

Acknowledgments

Authors acknowledge Dr. F. J. Galindo-Rosales for invaluable guidance in the experimental techniques.

References

[1] S. Martínez-Aranda, F. J. Galindo-Rosales, L. Campo-Deaño, Complex flow dynamics around 3D microbot prototypes. *Soft Matter*, **12**, 2334-2347, 2016.

[2] B. J. Nelson, I. K. Kaliakatsos, J. J. Abbott, Microrobots for minimally invasive medicine. *Annu. Rev. Biomed. Eng.*, **12**, 55-85, 2010.

[3] S. Martel, Magnetic Microbots to Fight Cancer, http://spectrum.ieee.org/robotics/medical-robots/magnetic-microbots-to-fight-cancer.

[4] W. Zhu, J. Li, Y. J. Leong, I. Rozen, X. Qu, R. Dong, Z. Wu, W. Gao, P. H. Chung, J. Wang, S. Chen, 3D-printed artificial microfish. *Adv. Mater.*, **27**, 4411-4417, 2015.

[5] O. Ergeneman, G. Chatzipirpiridis, J. Pokki, M. Marín-Suárez, G. A. Sotiriou, S. Medina-Rodríguez, J. F. Sánchez, A. Fernández-Gutiérrez, S. Pané, B. J. Nelson, In vitro oxygen sensing using intraocular microrobots. *IEEE Trans. Biomed. Eng.*, **59**, 3104-3109, 2012.

[6] M. J. Mack, Minimally invasive and robotic surgery. *J. Am. Med. Assoc.*, **285**, 568-572, 2001.

[7] M. C. Carrozza, P. Dario, L. P. S. Jay, Micromechatronics in surgery. *Trans. Inst. Meas. Control*, **25**, 309-327, 2003.

[8] M. Kohl, S. Abdelkhalik, S. Jeter, D. Sadowsk, A microfluidic experimental platform with internal pressure measurements. *Sens. Actuators, A*, **118**, 212-221, 2005.

[9] D. A. Ateya, A. A. Shah, S. Z. Hua, Impedance-based response of an electrolytic gas bubble to pressure in microfluidic channels. *Ses. Actuators, A*, **122**, 235-241, 2005.

[10] C. Y. Wu, W. H. Liao, Y. C. Tung, Integrated ionic liquid-based electrofluidic circuits for pressure sensing within polydimethylsiloxane microfluidic systems. *Lab Chip*, **11**, 1740-1746, 2011.

[11] K. Hosokawa, K. Hanada, R. Maeda, A polydimethylsiloxane (PDMS) deformable diffraction grating for monitoring of local pressure in microfluidic devices. *J. Micromech. Microeng.*, **12**, 1-6, 2002.

[12] P. Cheung, K. Toda-Peters, A. Q. Shen, In situ pressure measurement within deformable rectangular polydimethylsiloxane microfluidic devices. *Biomicrofluidics*, **6**, 026501, 2012.

[13] S. A. Berger, W. Goldsmith, E. R. Lewis, *Introduction to Bioengineering*, Oxford Univ. Press, Oxford, UK, 1996.

[14] Y. Xia, G. M. Whitesides, Soft Lithography. *Annu. Rev. Mater. Sci.*, **28**, 153-184, 1998.

[15] L. Campo-Deaño, M. S. N. Oliveira, F. T. Pinho, A review of computational hemodynamics in middle cerebral aneurysms and rheological models for blood flow. *Appl. Mech. Rev.*, **67**, 030801, 2015.